UNCLASSIFIED

AD **273 554**

Reproduced
by the

UNCLASSIFIED

273 554

62-2-6

THE SCATTERING OF 11 MEV - 19 MEV MONOCHROMATIC GAMMA RAYS

BY THE DEFORMED NUCLEUS, Ho^{165}

by

P. A. Tipler, P. Axel, N. Stein, and D. Sutton
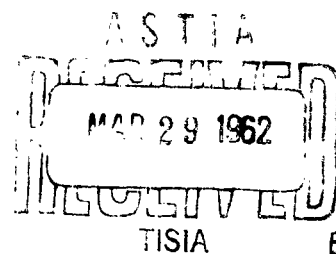
Technical Report No. 33

PREFACE AND ACKNOWLEDGMENTS

This report, which describes some improvements in the Illinois Bremsstrahlung Monochromator and the determination of the scattering of photons by holmium, was originally written as the Ph.D. thesis of Paul Allen Tipler.

We wish to thank Herbert Kuehne, Kongki Min, and Franca Kuchnir for their aid during this experiment. We also owe a debt to James O'Connell and Professor A. O. Hanson who contributed to the original development of the monochromator.

We are also indebted to Sim Um and his staff of operators at the 25 Mev betatron and to the personnel of both the machine shop and electronics shop.

<div style="text-align: right">

P. A. Tipler

P. Axel

N. Stein

D. Sutton

</div>

TABLE OF CONTENTS

ACKNOWLEDGMENTS

TABLE OF CONTENTS

CHAPTER I

INTRODUCTION

This thesis describes the measurement of the cross section at 135° for scattering of gamma rays by holmium. The experiment used the bremsstrahlung monochromator[1] at the University of Illinois 25 Mev betatron. A resolution of 0.6% and a maximum intensity of 10^4 gamma rays per second for each electron detector made it possible to look for structure in the giant resonance, and to compare the scattering cross section with the absorption cross section.[2]

The experimental apparatus, described in reference 1, was improved so that accurate and more detailed data could be obtained. The scattering cross section was measured at 48 energy points with an average precision of about 18%. The results show the following:

(a) A definite gross splitting of the giant resonance.

(b) No fine structure.

(c) Agreement in magnitude with the scattering measurement made by Fuller and Hayward[3,4] at 90°.

(d) Agreement with the energy dependence of the absorption data of Fuller and Hayward;[3] the magnitude of the absorption data seems to be about 19% too high.

(e) A slight preference for the three resonance fit to the absorption data over the two resonance fit. Zero point vibrations in the ground state would imply that the scattering data should agree with a three line fit even if only two different values existed for the three equilibrium axes.

OUTLINE OF THESIS

CHAPTER II

THEORY

A. The Giant Resonance and Deformed Nuclei

The outstanding characteristic of the nuclear photoeffect below meson threshold is the giant resonance. The general features[5] of the resonance can be characterized by the integrated absorption cross section, $\sigma_{int} = \int \sigma_{abs} \, dE$, the resonance energy, E_m, and the full width at half maximum, Γ. The integrated cross section and the resonance energy vary smoothly with atomic number A. Experimental data on the resonance energy are consistent with $E_m = 80 \, A^{-1/3}$ for $A > 40$, and with $E_m = 20$ to 23 Mev, roughly constant for $A < 40$.[6] The integrated absorption cross section is predicted by the electric dipole sum rule to be about 15 A Mev mb[5] (neglecting the factor of 1.4 due to exchange force contributions). The experimental cross section integrated over the giant resonance seems to exhaust the dipole sum; however, the absolute magnitudes of the experimental cross sections have been questioned recently leaving the factor of 1.4 very uncertain. Measurements with monoenergetic 17.6 Mev gamma rays indicate that the reported cross sections derived from measurements with bremsstrahlung spectra may be too high by about 30%.[7]

The absorption cross section is usually determined by summing the various partial cross sections,

$$\sigma_{abs} = \sigma(\gamma,n) + \sigma(\gamma,2n) + \sigma(\gamma,p) + \sigma(\gamma,\gamma) + \sigma(\gamma,\gamma') + \cdots \tag{1}$$

For heavy elements, the first two terms of Eq. (1) make up about 95%
of σ_{abs}, but the directly measured quantity is $\sigma(\gamma,n) + 2\sigma(\gamma,2n)$.
Uncertainties in the $(\gamma,2n)$ threshold and in the neutron multiplicities
add to the difficulties in determining σ_{abs} from photoneutron yields using
bremsstrahlung spectra. Although $\sigma(\gamma,\gamma)$ is only a few per cent of σ_{abs},
the two cross sections are directly related through the optical theorem
and dispersion relations as will be discussed in section B; therefore,
a measurement of $\sigma(\gamma,\gamma)$ can give information about the magnitude and
shape of σ_{abs}. The use of monochromatic photons avoids the difficulties
encountered in unfolding the bremsstrahlung spectrum. In addition, the
measurement of $\sigma(\gamma,\gamma)$ allows the use of the same detector to measure
the incident and scattered photons, thus avoiding complicated monitoring
calibrations.

The width, Γ, does not vary smoothly with atomic number, A.
Γ is smallest for nuclei with magic numbers of neutrons or protons,
and largest for nuclei with neutron or proton numbers farthest from the
magic numbers. The similarity of this behavior of the widths to that of
the quadrupole moments led Danos,[8] and Okamoto[9] to propose that
nuclear deformation was responsible for the variation in Γ from nucleus
to nucleus. The resonance energy is predicted to be inversely propor-
tional to the radius of the nucleus in the second form of the Golhaber-
Teller[10] hydrodynamical model and its extension by Steinwedel, Jensen,
and Jensen[11] in which the neutrons and protons oscillate as two separate
compressible fluids. For an axially symmetric deformed nucleus, this
model implies two resonant energies corresponding to oscillations along
the symmetry axis, and perpendicular to it. The difference in energies
is approximately proportional to the difference in the major and minor

axis of the spheroidal nucleus, R_1 - R_2. Okamato[12] has calculated the magnitude of the resonance splitting in the hydrodynamical model for various nuclei using the intrinsic quadrupole moments, Q_0, from Coulomb excitation probability to determine R_1 - R_2. He compares the experimental widths measured with poor resolution with $\Gamma = \Gamma_0 + \Delta \Gamma$, where Γ_0, the intrinsic width for spherical nuclei, is taken as 4.2 Mev, and $\Delta \Gamma$ is the difference in resonance energies. For strongly deformed nuclei, the experimental widths are larger than these calculated widths, indicating possibly that the intrinsic width is broadened. Up to now, calculations have omitted the effect of zero point vibrations. Single particle model calculations of the resonance splitting have been done by Wilkinson,[13] Soga and Fujita,[14] and Mottelson and Nilsson[15] using a deformed oscillator potential. In spherical shell model calculations, transitions of nucleons in the last filled shell carry most of the dipole strength; transitions of the valence nucleons play a minor role. In the zero range approximation that Brown, et al.[16,17] used in their calculation of the dipole state, the transitions from the closed shell nucleons contribute no width to the state; the valence particles presumably contribute appreciably to the width. The splitting of the resonance is essentially the same in either model, however, no detailed calculations of the intrinsic widths have been made.

The splitting of the giant resonance was first observed by Fuller and Weiss[18] for tantalum and terbium. The cross section $\sigma(\gamma, n) + \sigma(\gamma, 2n)$ was obtained from photoneutron yield data with corrections for the neutron multiplicity above the $(\gamma, 2n)$ threshold. The cross sections were fit by the superposition of two Lorentz shape resonance lines following the suggestion of Danos,[19] with the area under the higher energy line (corresponding to absorption along the two axes perpendicular to the

symmetry axis) twice that under the lower energy line. Splitting of the
giant resonance has since been experimentally observed in tantalum by
Spicer,[20] holmium and erbium by Fuller and Hayward,[3,4] and in
manganese and cobalt by Flournoy, Tickle, and Whitehead.[21]

It has been pointed out by Inopin[22] that the appearance of three
maxima in the region of the giant resonance would be the most direct
demonstration of the existence of non-axially symmetric nuclei. The
collective energy levels of non-axially symmetric nuclei have been
investigated by Davydov and Filippov[23,24] on the basis of the uniform
model of Bohr and Mottelson.[25] In this model, the deformation is given
by two parameters, β and γ. The axes of the ellipsoid used to approxi-
mate the shape of the nucleus are given by:

$$R_n = R_o \left[1 + \left(\tfrac{5\pi}{4}\right)^{1/2} \cos\left(\gamma + \tfrac{2\pi n}{3}\right)\right] \qquad (2)$$

for n = 1, 2, or 3. If γ = 0, the nucleus is a prolate ellipsoid of
revolution with n = 3 being the symmetry axis. For γ = 60°, the
nucleus is an oblate ellipsoid of revolution with n = 1 being the symmetry
axis. The maximum deviation from axial symmetry occurs for γ = 30°.
Values of the parameter, γ, are inferred for even A nuclei from experi-
mental values of the energies of the low lying collective levels which
correspond to rotational levels of deformed nuclei. These values of
can then be used to predict transition probabilities between these levels.
Although this model has had some success in explaining experiments,
there is considerable doubt that permanent non-axially symmetric deforma-
tions are necessary in regions of large deformation to explain the existing
experimental data on energy levels, and transitions between them. In
particular, the large zero point gamma vibrations obscure the meaning of
an equilibrium value of γ different from zero.[26,27]

Inopin extends the Danos and Okamoto calculations to the case of a non-axially symmetric nucleus and obtains:[22]

$$K_n = \frac{2.08}{R_n} \left[1 + \frac{R_n - R_o}{R_o} \right] \qquad (3)$$

where k_n is proportional to the frequency of oscillation along the axis R_n, and R_0 is the radius of the sphere of equal volume. He points out that the photoneutron data of Fuller and Weiss for terbium seem to indicate three maxima. Fitting their data to three equal area Lorentz lines, Inopin obtains deformation parameters of $\beta = 0.30$ and $\gamma = 19°$. This γ is somewhat higher than the $\gamma = 12°$ sometimes assigned to nuclei in this region of the periodic table. Fuller and Hayward[4] have been able to fit their $\sigma(\gamma, n) + \sigma(\gamma, 2n)$ data for holmium and erbium equally well with two lines or three lines. For their three line fit, they also obtain a relatively large γ of about 20°. (Since both the two line fit ($\gamma = 0$) and the three line fit ($\gamma = 20°$) are consistent with their data, there are probably other three line fits with smaller γ also consistent with their data.) They point out that the predicted scattering cross section is larger, especially at energies of 13 to 18 Mev, if three resonances are assumed rather than two. Their scattering data are not precise enough to distinguish between these two possibilities; furthermore, the absorption data from which the scattering cross section is calculated are uncertain for $E > 14$ Mev due to the unknown neutron multiplicity.

B. Cross Section for Photon Scattering

For a spherically symmetric nucleus the elastic scattering cross section in the forward direction is simply related to the total absorption cross section. If f(E) is taken as the forward scattering amplitude, the optical theorem gives:

$$\operatorname{Im} f(E) = \frac{E}{4\pi \hbar c} \sigma_a(E) \tag{4}$$

where $\sigma_a(E)$ is the total absorption cross section. The real part of f(E) is related to the imaginary part by the dispersion relation:[28]

$$\operatorname{Re} f(E) = \operatorname{Re} f(0) + \frac{2E^2}{\pi} P \int_0^\infty \frac{\operatorname{Im} f(E')}{E'(E'^2 - E^2)} dE' \tag{5}$$

where P stands for the Cauchy principle value of the integral and f(0) is the energy independent Thomson scattering amplitude $D = -\frac{Z^2}{A} \frac{e^2}{Mc^2}$. Combining Eqs. (4) and (5) gives:

$$\operatorname{Re} f(E) = D + \frac{E^2}{2\pi^2 \hbar c} P \int_0^\infty \frac{\sigma_a(E')}{E'^2 - E^2} dE' \tag{6}$$

The elastic scattering cross section in the forward direction is then

$$\frac{d\sigma_s(0°)}{d\Omega} = |f(E)|^2 = \left[\frac{E \sigma_a(E)}{4\pi \hbar c} \right]^2 + \left[D + \frac{E^2}{2\pi^2 \hbar c} P \int_0^\infty \frac{\sigma_a(E')}{E'^2 - E^2} dE' \right]^2 \tag{7}$$

If $\sigma_a(E)$ has the shape of a Lorentz line,

$$\sigma_a(E) = \frac{\sigma_m}{1 + L^2} \tag{8}$$

where $\qquad L \equiv \frac{E_o^2 - E^2}{E \Gamma}$

then

$$P \int_0^\infty \frac{\sigma_a(E')}{E'^2 - E^2} \, dE' = \frac{\pi}{2} \frac{L \, \sigma_a(E)}{E}$$

(9)

and

$$\frac{d\sigma_s(0°)}{d\Omega} = \left(\frac{E \, \sigma_m}{4\pi \hbar c}\right)^2 \left[\left(\frac{L}{1+L^2}\right)^2 + \left(\frac{L}{1+L^2} + \frac{D \, 4\pi \hbar c}{E}\right)^2 \right]$$

(10)

If the elastic scattering cross section is assumed to have the $(1 + \cos^2\theta)$ angular distribution characteristic of electric dipole scattering,

$$\frac{d\sigma_s(\theta)}{d\Omega} = \frac{1 + \cos^2\theta}{2} \frac{d\sigma_s(0°)}{d\Omega}$$

(11)

If the nucleus is not spherically symmetric, complications arise due to the possible dependence of the scattering amplitude on the relative orientation of the nucleus and the wave vector of the photon. Baldin[29,30] constructed a theory of the electric dipole polarizability of nuclei analogous to the theory of molecular polarizability.[31] He writes the electric dipole polarizability, α, as $\alpha = \alpha^S + \alpha^T$ where α^T, the tensor polarizability, depends on the orientation of the nucleus, while α^S, the scalar polarizability, does not. The elastic scattering cross section for unoriented nuclei averaged over photon polarizations in the initial state, and summed over final states is:

$$\frac{d\sigma_s}{d\Omega} = |F^T|^2 \frac{(2j+3)(j+1)}{j(2j-1)} \left[\frac{13 + \cos^2\theta}{40}\right] + |F^S + D|^2 \left[\frac{1 + \cos^2\theta}{2}\right]$$

(12)

where j is the spin of the nucleus, D is the Thompson amplitude and

$$F^T \equiv - \left(\frac{E}{\hbar c}\right)^2 \alpha^T$$

$$F^S \equiv - \left(\frac{E}{\hbar c}\right)^2 \alpha^S$$

The real and imaginary parts of F^T and F^S are connected by dispersion relationships similar to Eq. (5). The total absorption cross section for oriented nuclei and unpolarized photons is:

$$\sigma_a = \frac{4\pi\hbar c}{E}\left[\frac{3(j+1)}{2j-1}\left\{\frac{1}{6} - \frac{\overline{J_k^2}}{2j(j+1)}\right\}\text{Im}\,F^T + \text{Im}\,F^S\right] \qquad (13)$$

where $\overline{J_k^2}$ is the mean square projection of the nuclear spin on the photon wave vector. For unoriented nuclei, $\overline{J_k^2} = \frac{j(j+1)}{3}$ and Eq. (13) becomes:

$$\sigma_a = \frac{4\pi\hbar c}{E}\,\text{Im}\,F^S \qquad (14)$$

Thus the absorption cross section for unoriented nuclei is unaffected by the tensor polarizability, while the scattering cross section is increased by the spin dependent, nearly isotropic term,

$$\left|F^T\right|^2 \frac{(2j+3)(j+1)}{j(2j-1)} \frac{13 + \cos^2\theta}{40}$$

In order to evaluate Eqs. (12) and (14), a model must be used to calculate F^S and F^T which are proportional to the polarizabilities. For an axially symmetric nucleus, the polarizabilities in the laboratory system of coordinates are related to the "internal" polarizabilities in the coordinate system fixed to the nucleus and rotating with it by:[30]

$$\alpha^S(\text{Lab}) = \alpha_0^{\ S} \ (\text{nucleus})$$

$$\alpha^T(\text{Lab}) = \frac{j(2j-1)}{(j+1)(2j+3)} \ \alpha_0^{\ T}(\text{nucleus}) \tag{15}$$

If the nucleus is considered to be an aggregate of three linear oscillators of frequencies E_a/h, and $E_b/h = E_c/h$; damping Γ_A, and $\Gamma_B = \Gamma_C$, and strengths f_A, and $f_B = f_C$ then:

$$F_0^{\ T} = \frac{2}{3}\,(A - B)$$

$$F_0^{\ S} = \frac{1}{3}\,(A + 2B) \tag{16}$$

where

$$A = \frac{f_A}{\hbar c}\ \frac{E}{\Gamma_A}\ \frac{L_A + i}{1 + L_A^2}$$

$$B = \frac{f_B}{\hbar c}\ \frac{E}{\Gamma_B}\ \frac{L_B + i}{1 + L_B^2} \tag{17}$$

$$L_A = \frac{E_A^2 - E^2}{E\,\Gamma_A} \quad , \quad L_B = \frac{E_B^2 - E^2}{E\,\Gamma_B}$$

The elastic scattering cross section is then

$$\frac{d\sigma_s}{d\Omega} = \frac{j(2j-1)}{(j+1)(2j+3)}\ \left|\frac{2}{3}(A-B)\right|^2 \frac{13 + \cos^2\theta}{40} + \left|\frac{A+2B}{3}+D\right|^2 \frac{1 + \cos^2\theta}{2} \tag{18}$$

and the absorption cross section from Eq. (14) is

$$\sigma_a = \frac{1}{3}\ \frac{\sigma_A^{\ 0}}{1 + L_A^2} + \frac{2}{3}\ \frac{\sigma_B^{\ 0}}{1 + L_B^2} \tag{19a}$$

where

$$\sigma_A^0 \equiv \frac{4\pi f_A}{\Gamma_A} \quad , \quad and \quad \sigma_B^0 \equiv \frac{4\pi f_B}{\Gamma_B} \tag{19b}$$

Equations (12) and (18), derived by Baldin, apply to elastic scattering only. The cross section for inelastic gamma ray scattering to the ground state rotational band of deformed axially symmetric nuclei has been calculated by Maric and Mobius[32] using the Bohr-Mottleson[25] model. In this calculation, the projection, K_0, on the nuclear symmetry axis of the ground state spin I_0 changes by plus or minus one unit for transitions associated with oscillations perpendicular to the nuclear symmetry axis; K_0 does not change for transitions associated with oscillations along the symmetry axis. With the additional assumption that the energy spacing between states in the rotational band is small compared to the vibration energies, they obtain:[3]

$$\left(\frac{d\sigma_r}{d\Omega}\right)_{elastic} = \left| \frac{A+2B}{3} + D \right|^2 \frac{1 + \cos^2\theta}{2}$$

$$+ \left(I_0 2 K_0 0 | I_0 2 I_0 K_0 \right)^2 \left| \frac{2}{3}(A-B) \right|^2 \frac{13 + \cos^2\theta}{40} \tag{20}$$

$$\left(\frac{d\sigma_s}{d\Omega}\right)_{inelastic} = \left(I_0 2 K_0 0 | I_0 2 I_f K_0 \right)^2 \left| \frac{2}{3}(A-B) \right|^2 \frac{13 + \cos^2\theta}{40} \tag{21}$$

where I_0 and I_f are the spins of the ground and final states, K_0 is the spin projection on the nuclear symmetry axis, and A and B are given by Eq. (17) with the oscillator strengths evaluated using the dipole sum rule.[5] Since

$$\left(I_0 2 K_0 0 | I_0 2 I_0 K_0\right)^2 = \frac{\left[3 K_0^2 - I_0\left(I_0+1\right)\right]^2}{\left(2 I_0-1\right) I_0\left(I_0+1\right)\left(2 I_0+3\right)}$$

$$= \frac{I_0\left(2 I_0-1\right)}{\left(I_0+1\right)\left(2 I_0+3\right)}$$

for $K_0 = I_0$ in the Bohr-Mottleson model, Eq. (20) is identical to Eq. (18). Because of the sum rule:[31,3]

$$\sum_{I_f}\left(I_0 2 K_0 0 | I_0 2 I_f K_0\right)^2 = 1 \tag{22}$$

the sum of elastic plus inelastic scattering to the ground state rotational band is

$$\left(\frac{d\sigma_s}{d\Omega}\right)_{elastic+inelastic} = \left|\frac{A+2B}{3}+D\right|^2 \frac{1+\cos^2\theta}{2} + \left|\frac{2}{3}(A-B)\right|^2 \frac{13+\cos^2\theta}{40} \tag{23}$$

Note that Eq. (23) is the same as the classical average for elastic scattering which can be obtained from Eq. (18) by putting $j = \infty$. This can be used to extend Eq. (23) to non-axially symmetric nuclei. If a nucleus is assumed to be a system of three orthogonal oscillators, the classical cross section for electric dipole scattering of unpolarized gamma rays by unoriented nuclei is:[33]

$$\frac{d\sigma_s}{d\Omega} = \left|\frac{A+B+C}{3}+D\right|^2 \frac{1+\cos^2\theta}{2} + \left[|A-B|^2+|B-C|^2+|C-A|^2\right]\frac{13+\cos^2\theta}{180} \tag{24}$$

where A, B, and C are given by equations analogous to (17) and (19).

If C = B, Eqs. (24) and (23) are identical.

Although the elastic scattering cross section is dependent on the spin of the nucleus (if the contribution from the tensor polarizability is important), the calculation of Maric and Mobius implies that if the inelastic scattering to the ground state rotational band is included, the cross section is independent of the nuclear spin, and is given by the classical expression. The validity of this result is demonstrated by the measurements of Fuller and Hayward[4] of the scattering and absorption cross sections for Ho^{165} which has spin 7/2, and erbium of which 23% is Er^{167} with spin 7/2, and 77% even isotopes with spin 0. Both the absorption cross sections (measured by $\sigma(\gamma, n) + \sigma(\gamma, 2n)$) and the scattering cross sections were identical for the two elements indicating no marked dependence on the nuclear spin. Although the statistics and resolution of their scattering measurements were not good enough to exhibit the gross structure seen in the absorption cross section, their data clearly showed that the contribution from tensor polarizability is important.

It should be noted that all the calculations of the scattering cross section thus far are for static ground state shapes of the nucleus. The ground state vibrations of the nucleus imply additional scattering because of the increased average distortion seen by the photon. For example, the relatively slow γ vibrations (the zero point energies are of the order of tenths of an Mev) of an axially symmetric nucleus make the nucleus look axially asymmetric (on the average) to the 15 Mev photon.

CHAPTER III

MONOCHROMATOR PERFORMANCE AND IMPROVEMENTS

A. Introduction

The preliminary experiment which used the Illinois bremsstrahlung monochromator to measure the elastic scattering of photons by gold[1,2] provided information about which aspects of the monochromator needed improvement most. This chapter describes improvements and additional tests that were made, as well as the present status of the monochromator. In order to simplify the descriptions to follow, the operation of the mono-chromator will be reviewed briefly.

The experimental layout is shown in Fig. 1. The electron beam is extracted fromthe betatron and focused at F_1 by a double quadrupole magnet. The beam is then bent through an angle of 60° by the dispersion magnet (hereafter referred to as the D magnet), and refocused on a thin bremsstrahlung converter at F_2. In the converter, some electrons produce gamma rays which pass through a channel in a lead collimator and strike the scattering sample. Gamma rays scattered by the sample are detected by a 5-in. diameter, 4-in. thick NaI crystal coupled to an RCA 7046 photomultiplier. Residual electrons of energy E_e are de-tected by a 1.45 cm wide Pilot B plastic scintillator and photomultiplier after they go through the spectrometer (S magnet). A time coincidence between the gamma ray and electron detectors defines the energy of the incident gamma ray, $E\gamma = E_b - E_e$, where E_b, the energy of the
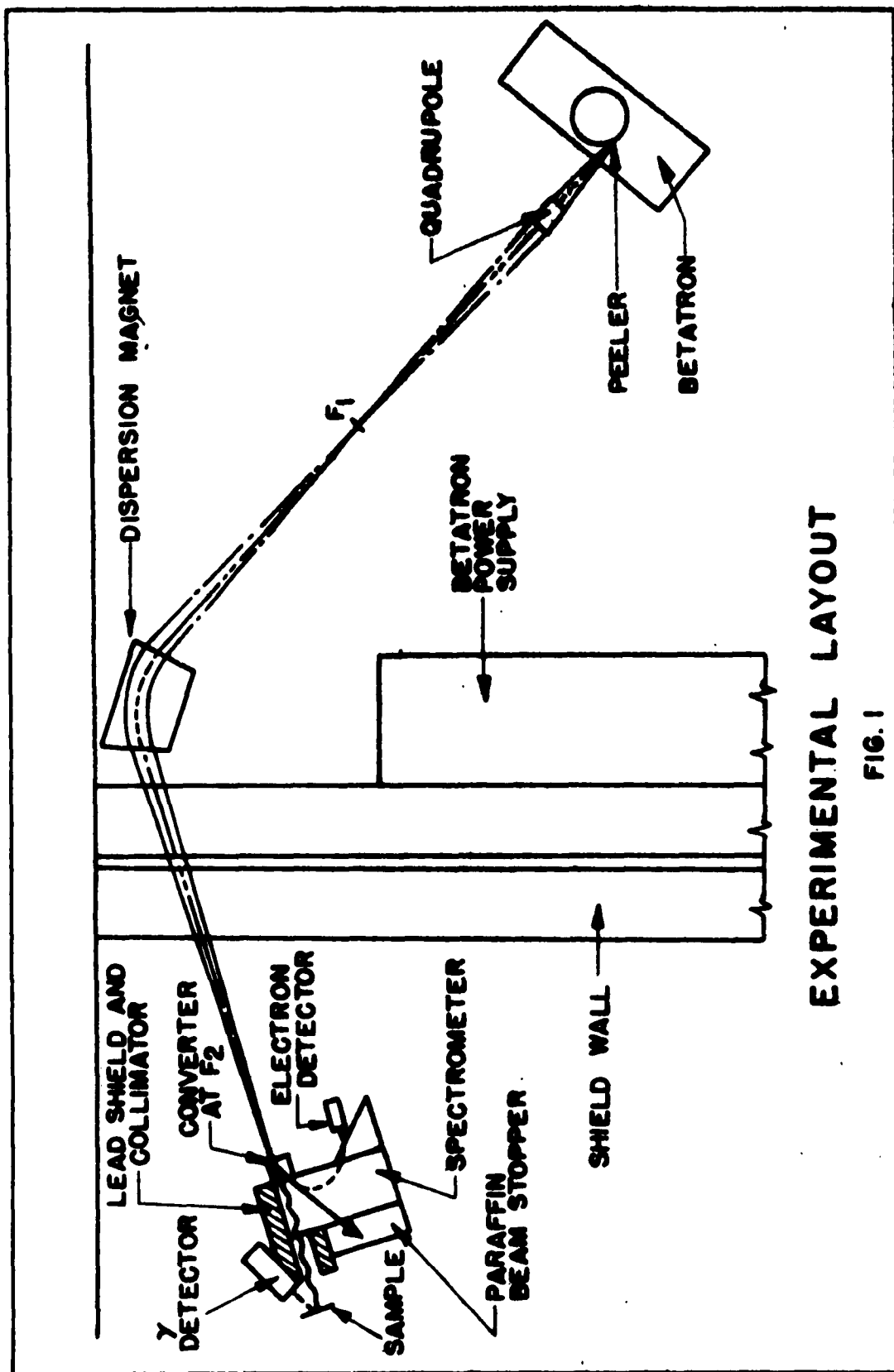
EXPERIMENTAL LAYOUT

FIG. 1

primary electron, is proportional to the magnetic field of the D magnet, and E_e is proportional to the magnetic field of the S magnet. The monochromator principle is illustrated in Fig. 2 for the typical values of E_b = 20 Mev, E_e = 5 Mev, and E_γ = 15 Mev. Because the converter is thin, most of the electron beam traverses it with a very small energy loss (about 15 kev), is bent slightly by the spectrometer, and is stopped in a paraffin beam stopper just outside the spectrometer. Three electron detectors are used with three coincidence circuits to measure simultaneously the scattering cross section at three different energies. A fourth coincident circuit, which has its timing mismatched, receives electron pulses from one of the detectors to measure the rate of chance coincidences. The coincident gamma ray pulse height spectra (associated with each of the three electron detectors or with the chance coincidence circuit) are displayed in four 25 channel groups of a 100 channel analyzer. The separation of the 100 channel analyzer into four 25 channel groups is accomplished by adding to the gamma ray pulse a pedestal pulse corresponding to channel 0, 25, 50, or 75 depending on which coincidence circuit is activated.

The limitation of this technique was the low counting rate which limited both the statistical accuracy of the data, and the precision of calibration experiments. The experiment with gold made it clear[1,2] that once some straightforward improvements were made, the precision with which a cross section could be measured in an experiment of reasonable length would depend on the background produced in the sample by non-monochromatic bremsstrahlung photons. The improvements that were made, and the present capabilities of the monochromator were governed by this limitation. Necessary monochromator improvements were pursued until each part of the system was better than would be needed for the attainable statistical accuracy. Furthermore, the system was made more convenient to operate both to speed data acquisition, and to enable assistants less familiar with the equipment to operate the system.

MONOCHROMATOR PRINCIPLE
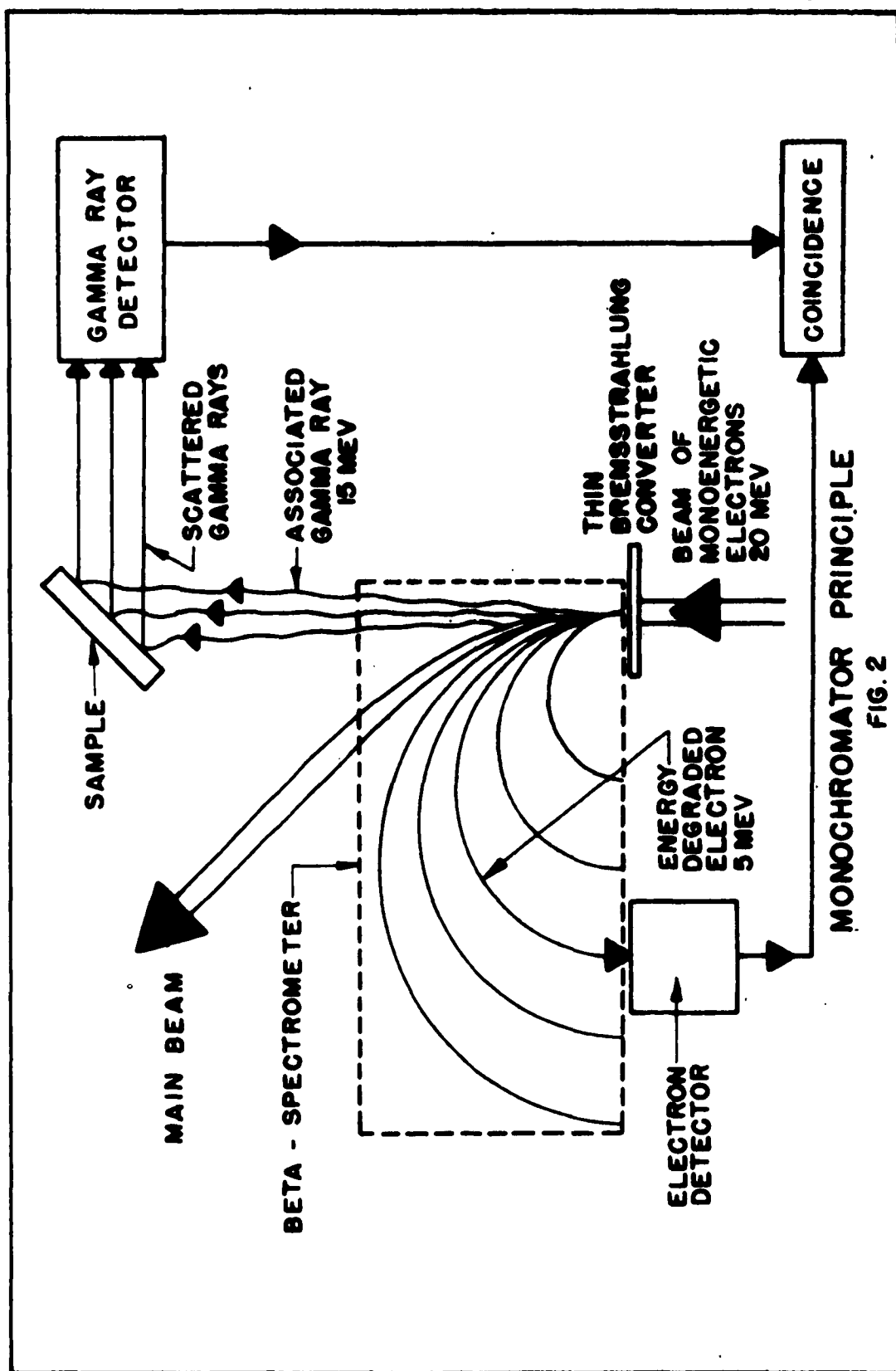
FIG. 2

The improvements and present performance will be described briefly in the order suggested by the system layout.

B. Betatron Operation and Beam Current

The beam intensity extracted at 20 Mev in the preliminary Au experiment had been greater than could be used in the scattering experiment due to the limitation placed on the useable intensity by the chance coincidence rate. However, more intensity was desirable for some calibration experiments, and a larger beam was needed at lower energies. It was also desirable to increase the duty cycle by extracting the beam over a longer period of time than the 150 microseconds used in the preliminary run. The beam intensity and pulse length depend on the betatron energy, the position of the stable electron orbit, the peeler position, and the expansion pulse in a complicated way that is not well understood. It was found, however, that the most important factor was the orbit position which could be varied by varying the gap between the betatron pole pieces with paper shims placed on the center and rim of the wafer, and on the legs of the return yoke. The best beam intensity and pulse length were obtained with shims of 15 mils on the wafer, and 40 mils on the legs. (The 25 mil difference on the legs is necessary to make the pole pieces fit tight mechanically. Additional shims of 5 mils at the center, and 10 mils at the rim were placed under the wafer for a better mechanical fit.) With these shims, a beam intensity of 10^{-8} amperes average current could be extracted at 20 Mev in a pulse which could be made flat for up to 400 microseconds using the longest expansion pulse available. At 10 Mev, 3×10^{-9} amperes could be extracted. The length of the beam pulse was not sensitive to the shape of the expansion pulse, although the shape of the beam pulse was. A change in the shims of 15 mils reduced the intensity by at least a

factor of 2, and made the beam pulse shape less stable. The optimum beam intensities and pulse shapes were obtained with the peeler at a slightly smaller radius for low energies. The limiting aperture at the entrance to the dispersion magnet reduced the current obtainable at the converter to about one half that extracted from the betatron.

The betatron energy regulator was improved so that it better compensated for the 6 cycle line voltage changes caused by the 300 Mev betatron. The regulator was also stabilized so that it would operate for long periods of time with only minor adjustments.

C. Energy Determination and Resolution

Since the betatron energy varies slightly during the extraction of the beam, the beam incident on the converter is not quite mono-energetic; however, this does not contribute to an energy spread in E_γ if the incident electrons are dispersed on the converter such that the different residual energies, E_e, which made gamma rays of a single energy, E_γ, were all focused at the same electron detector. This is accomplished by matching the dispersion of the D magnet at energy E_b to the dispersion of the S magnet at energy E_e. Prior to the start of this experiment the dispersions and focal properties of the D and S magnets were measured using a Li^7 ion source at F_1 of Fig. 1. The dispersion of the D magnet was found to be about 0.24%/cm, and that of the S magnet, about 1.06%/cm. Thus, when $E_b/E_e = 1.06/0.24 = 4.4$ the dispersions are matched to compensate for an energy spread in E_b. The Li^7 ion measurement was used also to calibrate E_b versus V_D, and E_e versus V_S, where V_D and V_S are the voltages of the Hall effect probes in the D and S magnets; however, the gamma ray energy, $E_\gamma = E_b - E_e$,

could be obtained more accurately in the region of the giant resonance of holmium from the known energies of the 15.11 Mev level[34] in C^{12} and the 11.4 Mev level[35] in Si^{28}. The energy scale for the holmium data was arrived at in the following way: Nearly all the data were taken with $E_b/E_e = 4.3$ as determined from the Li^7 measurement in order to match dispersions. A plot of V_D versus V_S for the scattering points taken very close to this ratio gave a curve which was very nearly a straight line. Two points on this line, $E_\gamma = 15.12$ Mev, and $E_\gamma = 11.4$ Mev for the middle electron detector were determined from scattering experiments with carbon and silicon. Knowing these two points, the other values of E_γ for this detector could be determined. Table I gives the values of E_γ for the middle electron detector, E_b (approximately), V_D, V_S, and the dates on which the holmium scattering data were taken at these energies. It would be surprising if the values of E_γ were in error by as much as 50 kev.

The relative energy spacing of the electron detectors and their resolution are measured by scattering gamma rays from the 15.11 Mev level in carbon. Figure 3 shows the coincidence counting rates for the three electron detectors as a function of spectrometer field measured by V_S. The primary electron energy is about 19.5 Mev. As the spectrometer field is increased, the 4.3 Mev electrons associated with the 15.1 Mev gamma rays are moved from one crystal to another. From Fig. 3, the resolution of each of the detectors is about 2.0% E_e, and the spacing about 2.7% E_e. Since $E_\gamma = 3.3 E_e$, this corresponds to a resolution of 0.6% E_γ and a spacing of 0.82% E_γ.

TABLE I

CHRONOLOGY OF DATA ENERGIES

E_γ	E_b	V_D	V_S	Date
12.49	16.3	10.95	09.43	April 25
14.50	19.0	12.55	10.83	April 27
11.00	14.4	09.76	08.47	April 28
15.46	20.2	13.30	11.35	April 30
13.50	17.6	11.75	10.08	May 1
11.73	15.3	10.34	08.92	May 2
18.21	23.8	15.50	13.17	May 4
15.12	19.7	13.04	11.20	May 17
15.12*	19.7	13.04	11.20	May 19*
15.98	20.9	13.73	11.68	May 19
14.01	18.3	12.16	10.41	May 21
16.99	22.2	14.53	12.36	May 22
17.92	22.2	14.53	10.20	May 22
13.01	17.0	11.36	09.76	May 23
11.99	15.7	10.55	09.12	May 24
18.90	23.0	15.00	09.76	May 25
15.98	20.9	13.73	11.68	May 27
16.50	21.6	14.14	12.04	May 28
15.46	20.2	13.33	11.39	May 29
08.01	10.6	07.38	06.57	May 31
07.08	10.6	07.38	08.70	June 1

*Converter and scattering geometry were changed just prior to
this run.
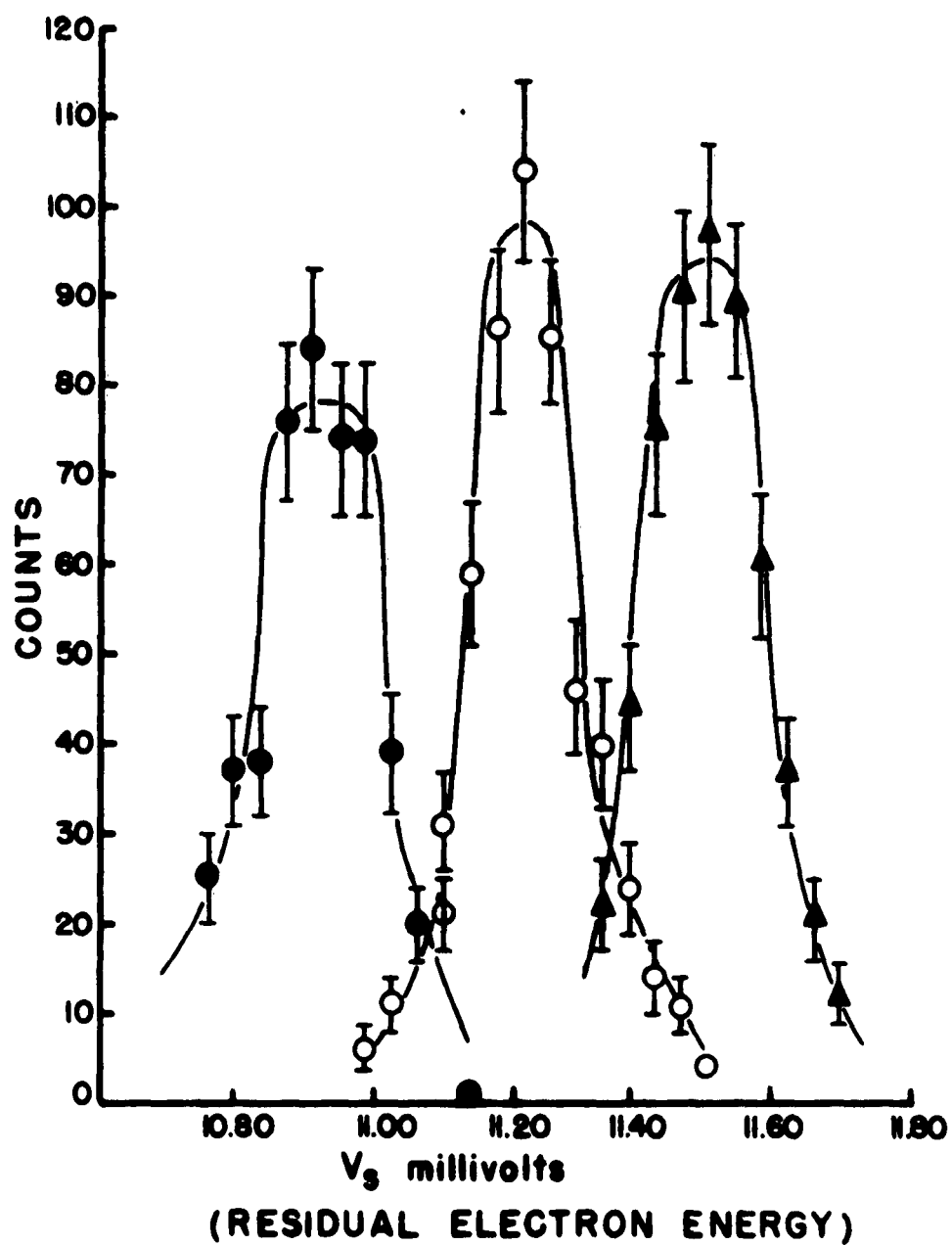
C^{12} RESOLUTION CURVES

FIG. 3

D. Bremsstrahlung Converter

The bremsstrahlung converter used in this experiment was a 1/2 mil tin foil, 7 cm wide, coated with a thin layer of willimite to make it scintillate when struck by the electron beam. The converter was placed at an angle of 40° to the electron beam; 40° is also the inclination of the focal plane of the spectrometer. The effective thickness of this converter, $\frac{0.0005 \text{ in.}}{\sin 40^o}$, is about 1.0×10^{-3} radiation lengths. The multiple scattering of electrons for this thickness is such that for $E_e = 3$ Mev, about 90% of the electrons are in a cone of half angle of $8^o.{}^{36}$ (Note that E_e was larger than 3 Mev even for $E_\gamma = 11$ Mev.) The non-radiative energy loss is about 15 kev. The effective width of the converter, (7 cm) $\sin 40^o$, is 4.5 cm measured perpendicular to the beam. The spatial spread of the electron beam depends on the pulse length and the dispersion of the D magnet. The energy of electrons extracted at time t, measured from t = 0 at maximum energy, is $E = E_0 \cos\omega t$, where E_0 is the maximum energy, and $\omega/2\pi$ is the betatron frequency, 180 cycles/sec. For small t, $E - E_0 = E_0(\omega t)^2/2$. Using 0.24%/cm for the dispersion of the D magnet, the 4.5 cm converter spans all the electrons extracted from t = - 130 microseconds to t = 130 microseconds corresponding to a 260 microsecond beam pulse. If monoenergetic electrons were focused to a point on the converter, the distribution of electrons on the converter would be proportional to $N_t x^{-1/2}$ where N_t is the distribution of electrons in time, and x is measured perpendicular to the beam from x = 0 where electrons of maximum energy, E_0, strike the converter. The relative number of electrons at x in dx, $N_x dx$, assuming the distribution of monoenergetic

electrons to be a Gaussian with a 1/e width of 0.5 cm, is shown in Fig. 4 for dx = 0.5 cm, and the usual beam pulse (N_t = constant for - 150 micro-seconds < t < 150 microseconds and N_t = 0 for all other t).

E. Stability of Monochromator Efficiency

Every electron that originates in the converter and is detected in the electron counter has associated with it a photon which leaves the converter at the same time. It is important to know the probability that this photon (1) hits the sample, (2) is scattered into the gamma detector, and (3) produces a pulse which is counted as a true coincidence. In order to determine factors (1) and (3), an auxiliary measurement is made in which the gamma ray detector is placed in the main photon beam (with the yield greatly reduced) such that it intercepts the gamma rays which would be incident on the sample in the scattering measurement. Except for corrections due to edge effects of the crystal (which can be absorbed in the effective solid angle), the number of coincidences per electron detected in this "bremsstrahlung measurement" measures factors (1) and (3). A lead collimator was constructed so that it, rather than the sample size, determines the number of photons which hit the sample. In the bremsstrahlung position, the NaI crystal intercepts this same group of photons.

Figure 5 shows the spectra of coincident gamma rays obtained in a typical bremsstrahlung measurement. The first three spectra are associated with the three electron detectors, and are obtained simultaneously in about 5 minutes during which about 8,000 electrons reached each detector. The fourth spectrum is not obtained at the same time because the fourth coincidence circuit measures only chance coincidences.
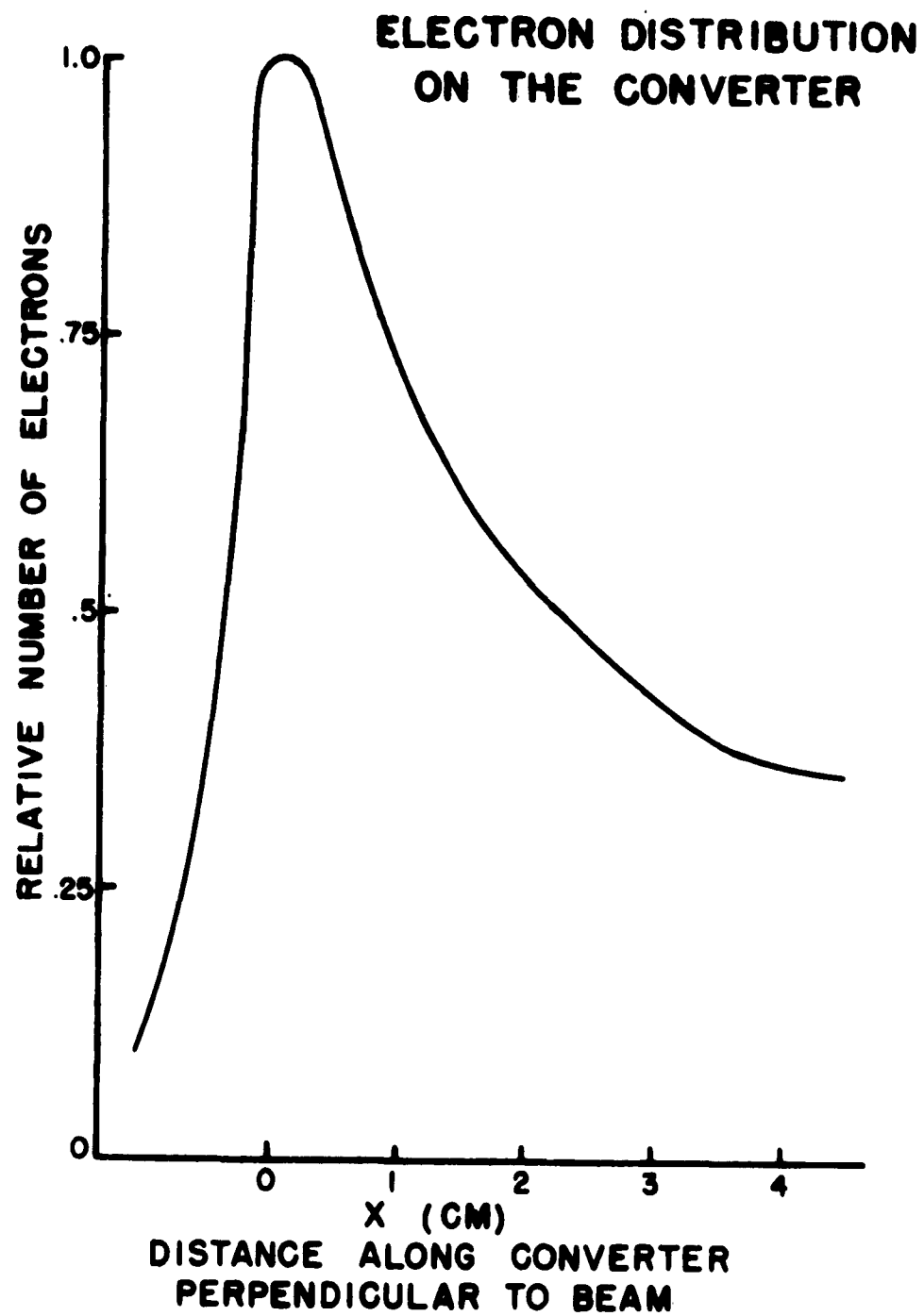
ELECTRON DISTRIBUTION
ON THE CONVERTER

RELATIVE NUMBER OF ELECTRONS

X (CM)
DISTANCE ALONG CONVERTER
PERPENDICULAR TO BEAM

FIG. 4

4 COUNTER BREMSSTRAHLUNG SPECTRA

FIG. 5
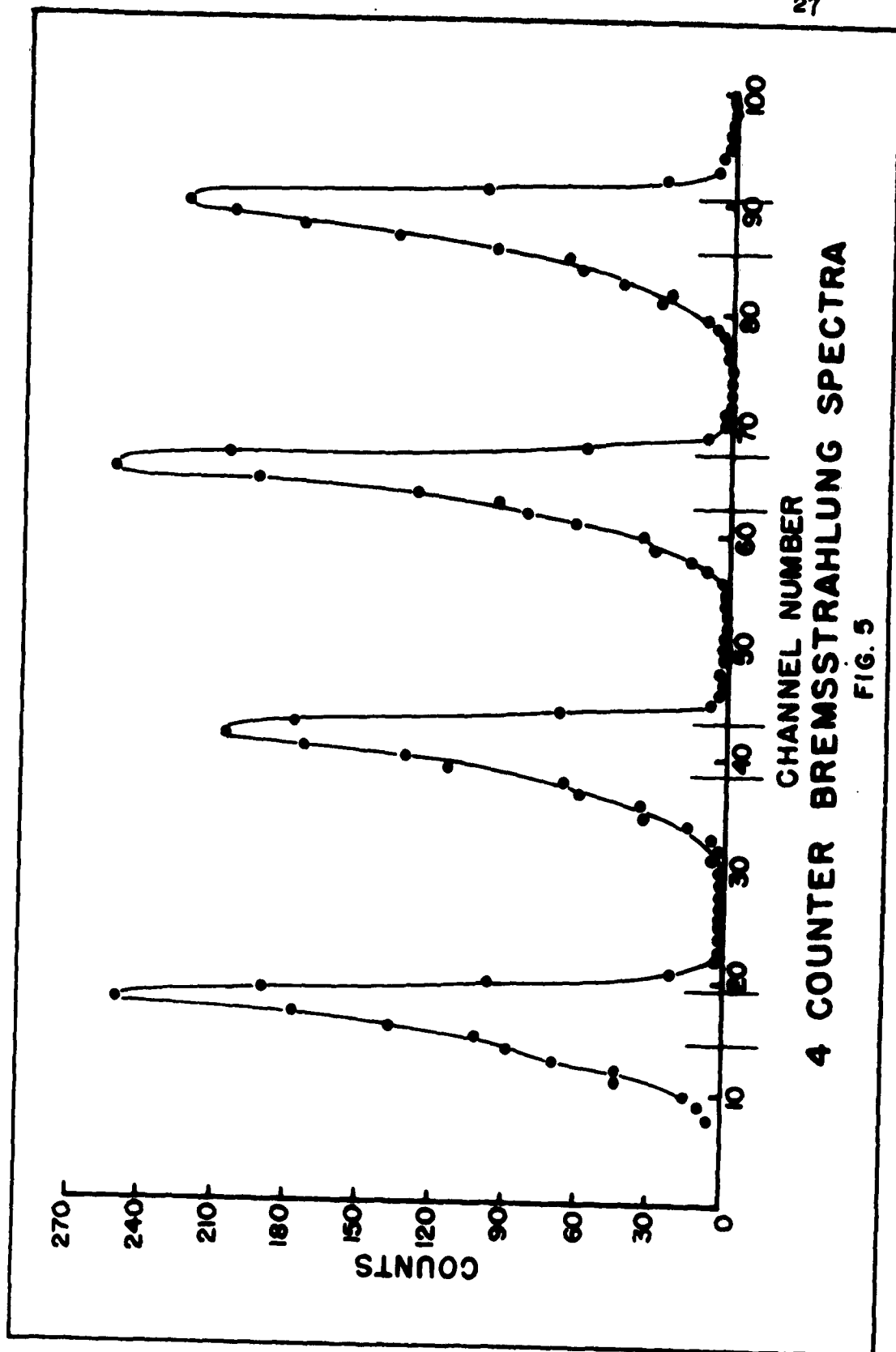
(The electron counting rate is so low in the bremsstrahlung measurement that no chance coincidences are recorded.) The fourth spectrum is obtained in an additional run for which the relative cable delays are adjusted so that the fourth coincidence circuit receives truly coincident pulses. Because of the energy dependence and magnitude of the background spectrum, only pulses in the photopeak are used to obtain the scattering data. The vertical lines on the x axis in Fig. 5 show the useable channels in each group. The number of coincidences in these channels per detected electron is called the bremsstrahlung efficiency. Since this efficiency is used directly in computing the cross section from the scattering data, it is important to know what factors affect it, and how sensitive it is to the various fluctuations that might occur during a scattering run. The remaining portion of this section describes the conceivable difficulties which are divided into those which might be caused by unpredicted electronic behavior, and those which would be due to a geometric shift of the gamma ray beam. The analyses and experiments which will be presented confirm the reliability of the bremsstrahlung efficiency measurements.

One important comparison which was made involved the relative efficiencies of the four coincidence circuits (and the three electron detectors). In order to allow for variations in electronic components, each coincidence circuit was followed by its own discriminator. These were adjusted individually to reject singles pulses, but to detect relatively small coincidence pulses. Possible changes in parameters would have been expected to influence only the effective resolving time, which will be discussed below. Inasmuch as no precautions were taken to be sure that all coincidence circuits were identical, it is likely that one of the circuits would be most sensitive to a wide variety of fluctuations. It was therefore

very reassuring to find that the relative fluctuations observed between the various outputs were both small and random. These fluctuations were almost always consistent with expected statistical accuracy (of about 3% per group per run). The slight evidence for fluctuations outside of statistics could have been due to minor changes in effective electronic biases; these fluctuations were small enough to have had negligible influence on the final results (except for the runs at E_γ = 19 Mev, for which the quoted experimental error was increased to allow for the implied uncertainty).

In order to guarantee the proper timing of the pulses to the coincidence circuits, the resolving time of each coincidence circuit was measured by varying the relative cable delay between the electron and gamma ray counters, and plotting the bremsstrahlung efficiency versus cable delay. Figure 6 shows a typical cable curve. The full width at half maximum, $2\tau = 3.0$ meters, corresponds to 1.2×10^{-8} seconds (1.0×10^{-8} seconds was more typical). This resolving time is determined by the length of the shorting stubs on the electron and gamma ray detectors, and the coincidence discriminator bias setting. These parameters were chosen to give the smallest resolving time without decreasing the efficiency or making the efficiency critically dependent on biases. The broad flat maximum and the steep sides in Fig. 6 indicate that possible changes in effective timing due to gain or bias shifts would not be expected to introduce errors.

Due to the relatively slow rise time of the pulses from the NaI detector, small pulses take longer to activate the coincidence circuit than do larger pulses; therefore, when the cable delays are adjusted so that pulses in the photopeak are in coincidence, smaller pulses from coincident gamma rays may arrive too late. It is important
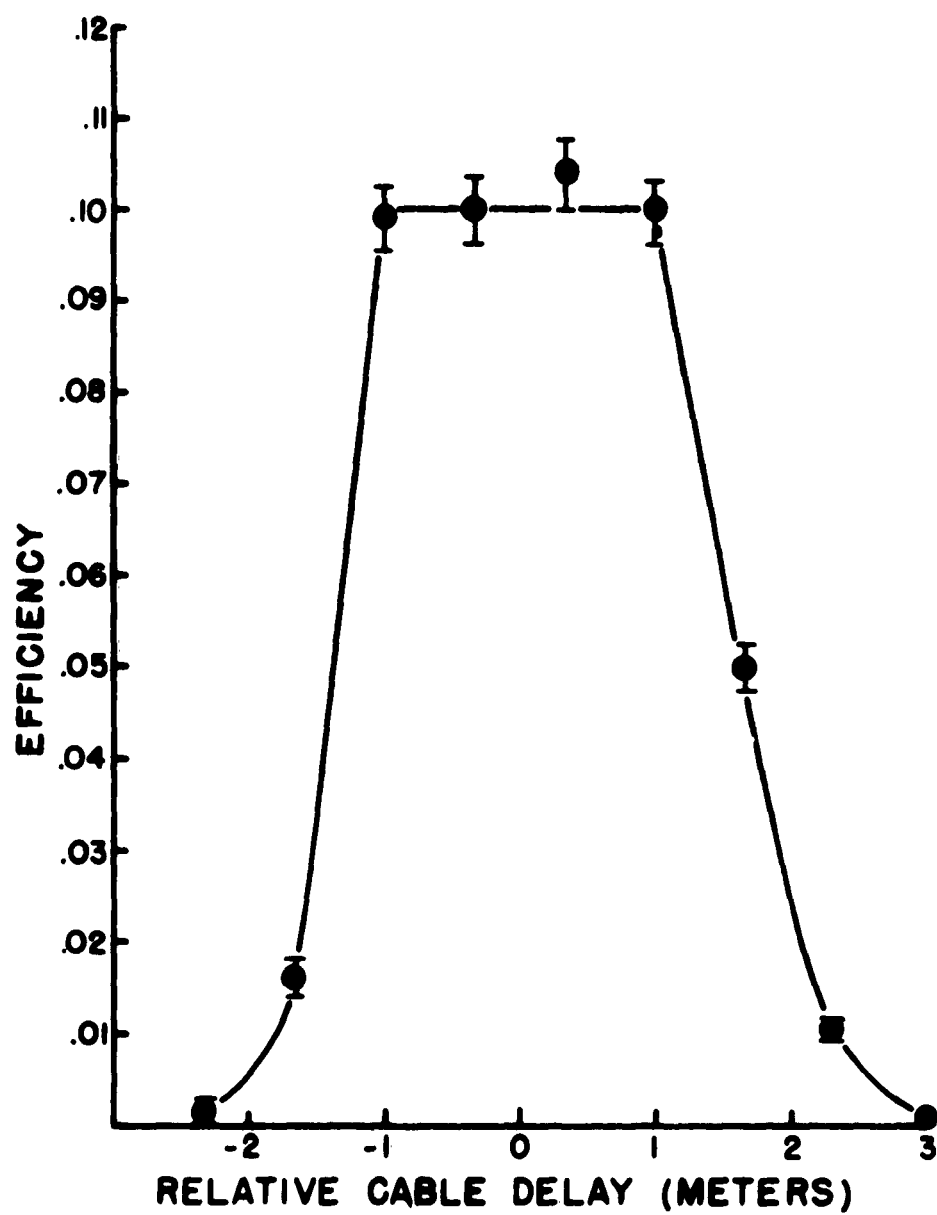
COINCIDENCE RESOLVING TIME

FIG. 6

to remember that these pulses which are smaller in amplitude are amplified and limited before they reach the coincidence circuit so that their duration is independent of their amplitude. The solid line in Fig. 7 shows the spectrum of coincident gamma rays obtained with the resolving time used during the data runs of about 10^{-8} seconds. The dashed line is the spectrum obtained with a resolving time long enough (about 4×10^{-8} seconds) so that all coincident gamma ray pulses are displayed. (Pulses corresponding to less than 3 or 4 Mev energy loss in the NaI crystal are below the bias of the discriminator which precedes the coincidence circuit; channel 50 corresponds to energies above those needed to activate the coincidence circuit.) Note that the number of pulses in the photopeak is the same to within statistics in both cases. Since the bremsstrahlung efficiency does not increase when 2τ is increased from 10^{-8} seconds, the efficiency cannot depend critically on bias or gain shifts in the relevant circuits for $2\tau = 10^{-8}$ seconds.

The fact that the very low energy pulses do not appear in coincidence in Fig. 7 makes possible another important stability check related to chance coincidence background. If anything produced a slow effective variation of 2τ in one of the circuits, the main error in the overall measurement would be caused by incorrect chance background subtraction. The very low channels, however, provide an excellent, continuous measure of the chance coincidence background because they do not record true coincidences. In the entire group of experiments, no anomalies were found that could be associated with relative fluctuations of the chance coincidence rates by the different circuits.

A further check on the internal consistency of the bremsstrahlung efficiency was made by comparing the predicted variation with energy with the observed energy dependence. The bremsstrahlung efficiency
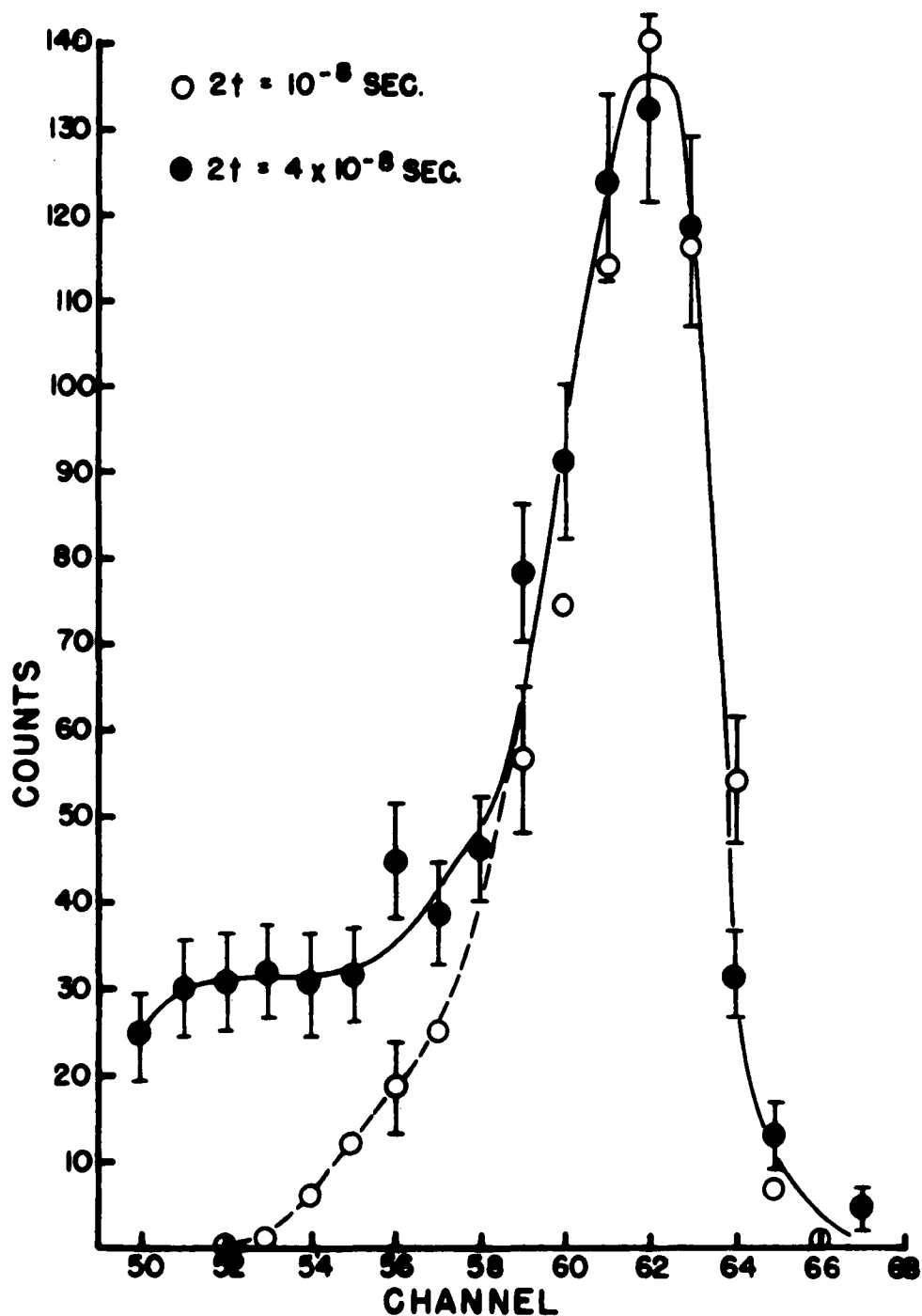
BREMSSTRAHLUNG SPECTRA FOR
TWO DIFFERENT RESOLVING TIMES

FIG. 7

depends on energy for three reasons. (1) The angular spread of the gamma ray beam due to multiple scattering of the electrons in the converter, and the intrinsic angular spread of bremsstrahlung vary inversely with E_b; therefore, more gamma rays should hit the crystal for higher E_b. (2) The detection efficiency of the NaI crystal increases with higher values of E_γ . (3) The timing of the gamma ray pulses depends on the pulse height due to the rise time effect discussed above. In order to compensate for (3), the gain of the gamma ray detector is adjusted at each new energy so that the coincident gamma ray pulse height of interest is always the same. The fact that the delay dependence of cable curves taken for low energies is identical to Fig. 6 which was taken at high energy indicates that the efficiency is still not critically dependent on biases.

Figure 8 shows the dependence of the bremsstrahlung efficiency on E_b. Except for the 22.2 Mev and 23 Mev points, the gamma ray energy was 0.765 E_b. The solid curve is drawn through the experimental points (+) which were all taken on two consecutive days. The open circles are points which were measured at various times throughout the experiment over a period of about six weeks. Statistical errors which are not shown were about 2%. The dashed curve is an estimate of the fraction of the gamma rays emitted at the converter which interact with the crystal. This curve is normalized to the experimental curve at 16 Mev. To obtain the fraction of gamma rays that hit the crystal, the angular distribution appropriate to the effective converter thickness was taken from the calculations of Miller[37] who used a Gaussian function for the angular distribution of multiply scattered electrons, and the intrinsic bremsstrahlung angular distribution given by Gluckstern and Hull.[38] The interaction probability
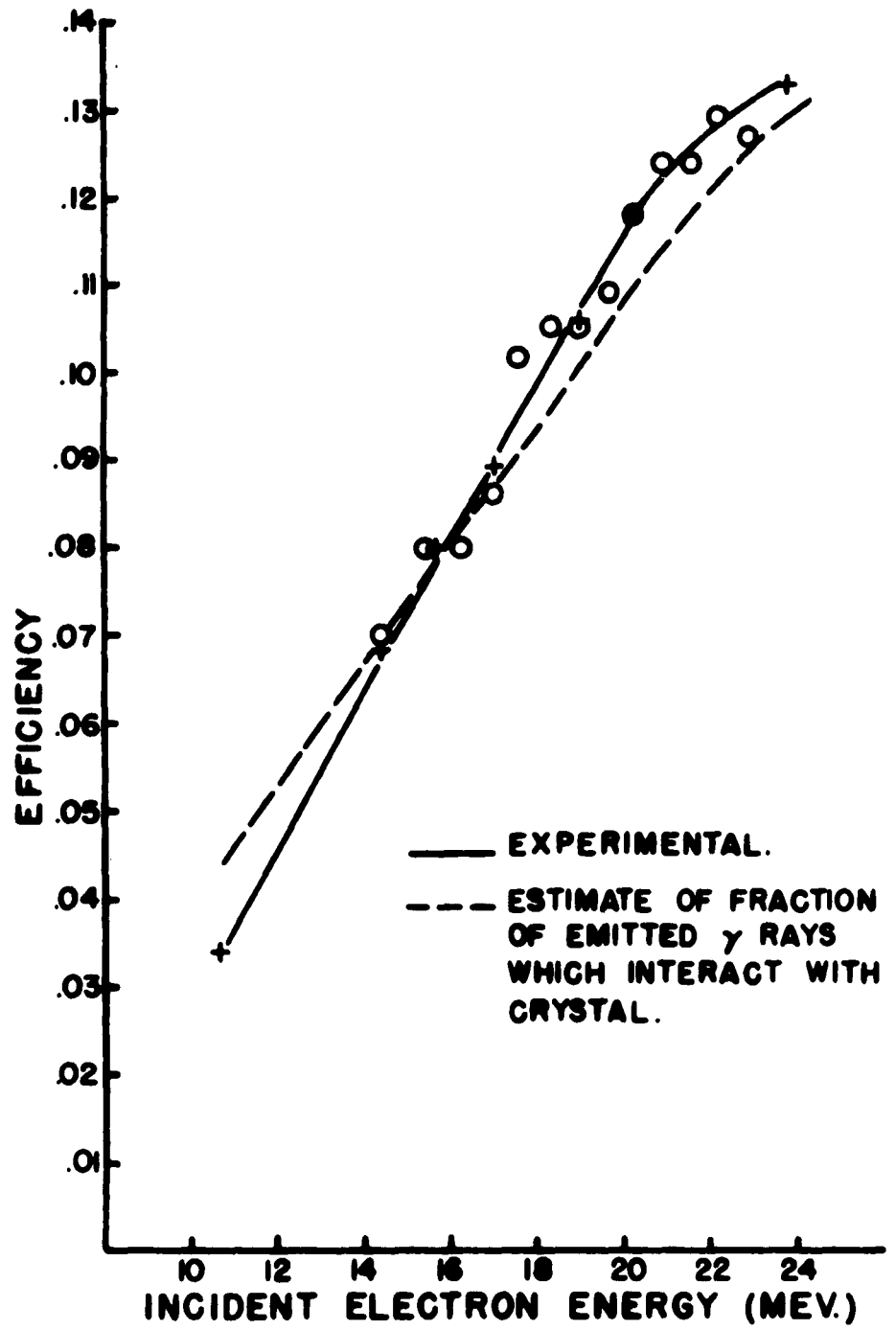
BREMSSTRAHLUNG EFFICIENCY VS ENERGY

FIG. 8

was taken as $(1 - e^{-\mu L})$, where L is the crystal length, and μ(E) for NaI was obtained from the tables of G. White Grodstein.[39] Corrections to this estimate for the extension of the source due to the distribution of electrons on the converter, and for the angle of the cone of interacting gamma rays being somewhat smaller than that defined by the crystal due to the lead collimator would increase the slope of the estimated curve bringing it into better agreement with the experimental curve. In view of the reasonable agreement between this estimate and the experimental curve, the variation of the bremsstrahlung efficiency with energy is probably almost entirely due to these factors. This agreement helps eliminate the possibility of unsuspected sensitivity to bias or systematic energy dependent errors.

The geometric position of the electron beam on the converter can vary due to changes in (1) the maximum energy of the electrons from the betatron, (2) the magnetic field in the D magnet, or (3) the time distribution of electrons in the pulse. The beam monitoring system during a scattering run is sensitive to any of these changes, but it is important to know whether a detected change implies an error large enough to make the data useless. Furthermore, during a measurement of bremsstrahlung efficiency, the electron counting rate is so low as to make detailed monitoring of the geometric beam position difficult. It is easier to make the bremsstrahlung efficiency insensitive to beam position, and use only crude monitoring.

The effective bremsstrahlung efficiency as a function of beam position was measured in two ways, and is shown in Fig. 9. The edges of the converter during normal operation are shown by the vertical lines along the beam position axis; the highest energy electrons normally strike at 0 on the abscissa scale. The crosses in Fig. 9 represent the measured bremsstrahlung efficiency obtained with a time shortened pulse which was

about 30 microseconds long, and produced a 1 cm diameter beam on the converter. The experimental points were taken by varying the D magnet in steps of about 0.2% corresponding to displacements of 0.8 cm perpendicular to the beam. (The converter was moved during the measurement so that the entire beam was always on the converter.)

The circles in Fig. 9 were obtained with the same beam arrangement but by measuring the scattering rather than the bremsstrahlung efficiency. These data are more crude than the bremsstrahlung efficiency data because they correspond to a wider, somewhat uncertain gamma ray energy interval. (The data represent scattered photons of about 15 Mev when a Pb sample was used without any monochromatic requirements; all gamma ray pulses of the correct size were recorded without using the coincidence circuits.)

Figure 9 shows that the efficiency is relatively constant over a 2 cm interval and falls when the beam moves in either direction from that interval. The decrease in efficiency is due to gamma rays which do not reach the target (or crystal) because they are stopped in the collimator.

The average bremsstrahlung efficiency can be calculated, numerically, from the known electron distribution on the converter (Fig. 4), and the bremsstrahlung efficiency as a function of beam position (Fig. 9). For the converter subtending 4 cm perpendicular to the beam, and the normal beam position, variations in position as large as 1 cm would decrease the bremsstrahlung efficiency by only 3%. Shifts of beam position of 1 cm would be very easily detected by the position monitor, and occurred only as very rapid transients when large power surges were produced by the 300 Mev betatron. The earlier scattering runs (see Table I) were taken with a converter subtending 5.8 cm perpendicular to the beam and with the nominal beam position at +1 cm (rather than 0) on the abscissa of
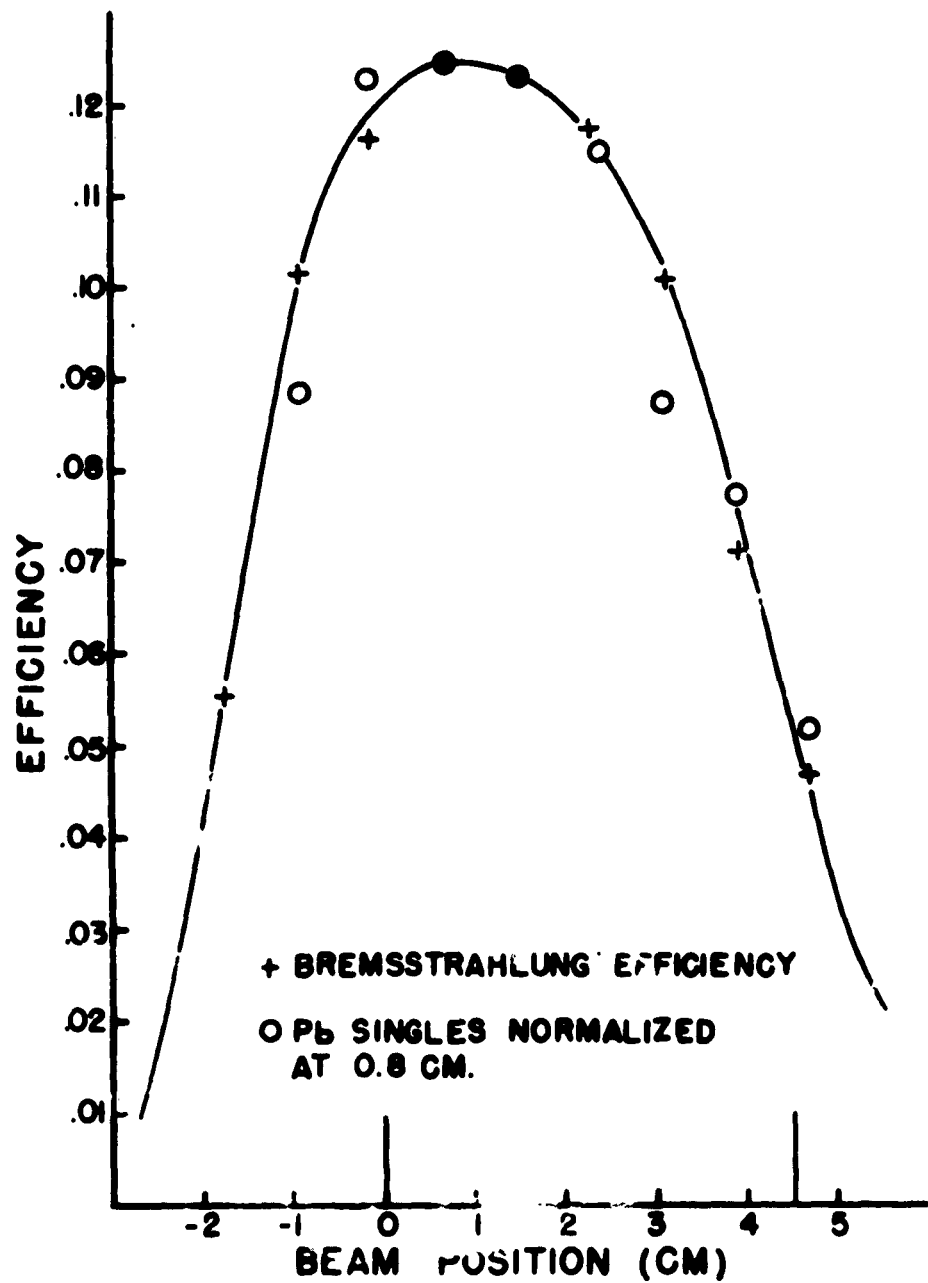
BREMSSTRAHLUNG EFFICIENCY
VS BEAM POSITION

FIG. 9

Fig. 9. Under these less favorable conditions, a shift of the beam to 0 would have caused a 6% increase, and a shift to +2 would have caused a 12% decrease.

As can be seen from Fig. 9, if the high energy edge of the beam were positioned at 0, a longer beam pulse and wider converter would not add significantly to the counting rate with the collimation used since the efficiency is so low for electrons which strike beyond +4.5. A longer beam pulse and wider converter might add to the counting rate if the high energy edge of the beam were positioned at -1 or -2 cm; however, the average efficiency would then depend critically on the beam position, and the beam would not be at a maximum efficiency position. The efficiency curve of Fig. 9 could be broadened by enlarging the collimator; however, in order to take advantage of the additional gamma rays, the sample would have to be larger, and unless a larger crystal were also used, the convenience of the crystal and sample intercepting the same group of photons in the bremsstrahlung and scattering measurements would be lost. Thus, although the electron beam can now be extracted in a 400 microsecond pulse, only about 260 microseconds (giving a 4.5 cm wide beam at the converter) can be used during precise measurements due to the efficiency limitation.

The broad maximum and symmetry of the average bremsstrahlung efficiency shows, incidentally, that the crystal and scattering sample are illuminated symmetrically about a vertical line through their centers. This conclusion was checked independently, though crudely, by measuring the bremsstrahlung efficiency for different parts of the crystal (by shielding other parts).

F. Monitoring Devices

The principal monitors of the incident gamma ray intensity were the electron scalers which recorded the number of secondary electrons from the converter. New 50 megacycle scalers were built to count these pulses from the electron detectors. The energy of the incident photons was monitored by periodic checks of the voltages, V_D and V_S, of the Hall effect probes in the D and S magnets. The main part of this section deals with the checks that were available on the geometric position of the primary electron beam.

In order to minimize the number of chance coincidences, it was desirable to keep the yield as steady as possible. The yield from the betatron could be monitored by the betatron operator using an ionization chamber in the gamma ray beam produced by the part of the internal beam not extracted hitting the injector. The ionization chamber current was very nearly proportional to the extracted beam current. (A scope display of the output of a scintillator and photomultiplier placed in this same beam gave a good indication of the shape of the beam pulse.) The counting rate of a few counts per second of the mechanical registers following the electron scalers provided an audible monitor of the yield striking the converter. A rate change could be produced either by a change in the main beam intensity or a shift of part of the beam off the converter. A check of either the betatron operator's intensity monitor or one of the beam position monitors (to be described below) indicated which was the cause.

The position of the beam on the converter could be observed by looking at the scintillations of the especially coated converter. The beam position could also be determined from the scope display of pulses from an unused dynode of the photomultiplier of one of the electron detectors.

Figure 10(a) is a sketch of the scope display. The display covers a narrow time interval near the time when the betatron energy was a maximum; this time is known accurately. The pulses at t_1 and t_5 are due to very low energy primary electrons hitting the brass walls of the vacuum pipe and producing many secondary electrons which get into the detector. Background from these non-converter electrons and gamma rays is eliminated by sensitizing the electron scalers and gamma ray pulse height analyzer only from times t_2 to t_4. Secondary electrons at times t_2 and t_4 are due to primary electrons of the same energy from early and late parts of the beam pulse hitting the low energy edge of the converter. (t_2 is 130 microseconds before the maximum energy, while t_4 is 130 microseconds after this maximum.) Primary electrons having the maximum energy hit the high energy edge of the converter, and produce secondaries at time t_3. If the betatron energy increases slightly, the maximum energy electrons miss the converter, and there is a gap at t_3 as in Fig. 10(b). A shift of 1/2 cm corresponding to a betatron energy increase of 0.1% throws 33% of the beam off the converter (see Fig. 4), and is easily detected. It also can be heard because there is a 33% decrease in the counting rate in the electron scalers. On the other hand, a shift toward lower energy is less noticeable since it does not produce an audible change; it does shorten the duration of the converter pulse, and it increases the edge pulses at t_1 and t_5 as in Fig. 10(c). A 2 cm shift shortens a 260 microsecond pulse by 25%. For detecting shifts toward lower energy, it was necessary to rely on the betatron operator's energy monitor (which was good to 0.1%), or on visual checks of the beam position. It was convenient to occasionally increase the energy of the betatron slightly to see if the beam was on the edge of the converter. Another, less direct, check on the beam position was made by noting the

(a)

t_1 t_2 t_3 t_4 t_5

(b)

t_1 t_2 t_3 t_4 t_5

(c)

t_1 t_2 t_3 t_4 t_5

TIME AXIS
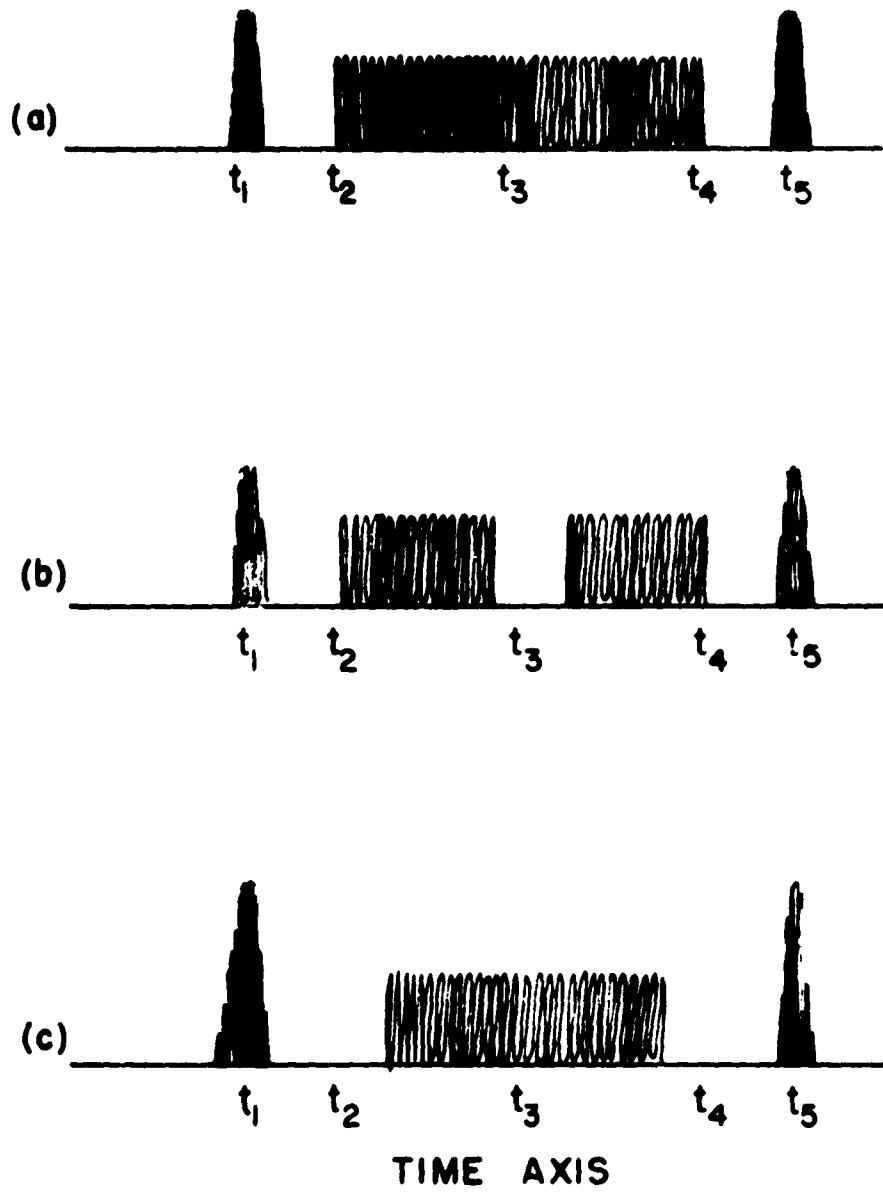
DISPLAYS ON
MONITORING OSCILLOSCOPE

FIG. 10

betatron energy and yield pulse shape at the same time that V_D and V_S were checked. (The beam position could not change unless there was a change in the betatron energy, the timing or shape of the yield pulse, or the field of the D magnet.)

Since the efficiency change was about 3% for a 1 cm change in beam position, with this monitoring system the efficiency never changed by more than 3%, and the average efficiency was probably within 0.5% of the maximum value. For the earlier data taken with the larger converter, the efficiency was more dependent on beam position, and since the normal position was not on the edge of the converter, small shifts toward higher energy were not as noticeable. For these data, the average efficiency might vary as much as 3% from that measured in the bremsstrahlung runs.

G. Calculation of the Absolute Efficiency

In this section the calculation of the monochromator efficiency necessary to determine the absolute cross section from the data will be described. The scattering sample was 912 grams of holmium oxide contained in a thin walled aluminum box, 10 cm high, 14 cm long, and 5 cm thick. The sample was placed so that its normal bisected the 45° angle between the gamma ray beam and the crystal axis. The 5 in. diameter by 4 in. thick NaI crystal was 20.3 cm from the center of the sample for most of the scattering runs. A one inch thick aluminum disc was placed on the face of the NaI crystal to absorb very low energy gamma rays. The scattering geometry is shown in Fig. 11.

Consider an element of the sample of area, dA, and thickness, dx, located at a depth, x, in the sample. The number of true coincidences counted due to this element, N_t, is proportional to: (1) the number of electrons detected, N_e, (2) the probability, P_γ, per detected electron
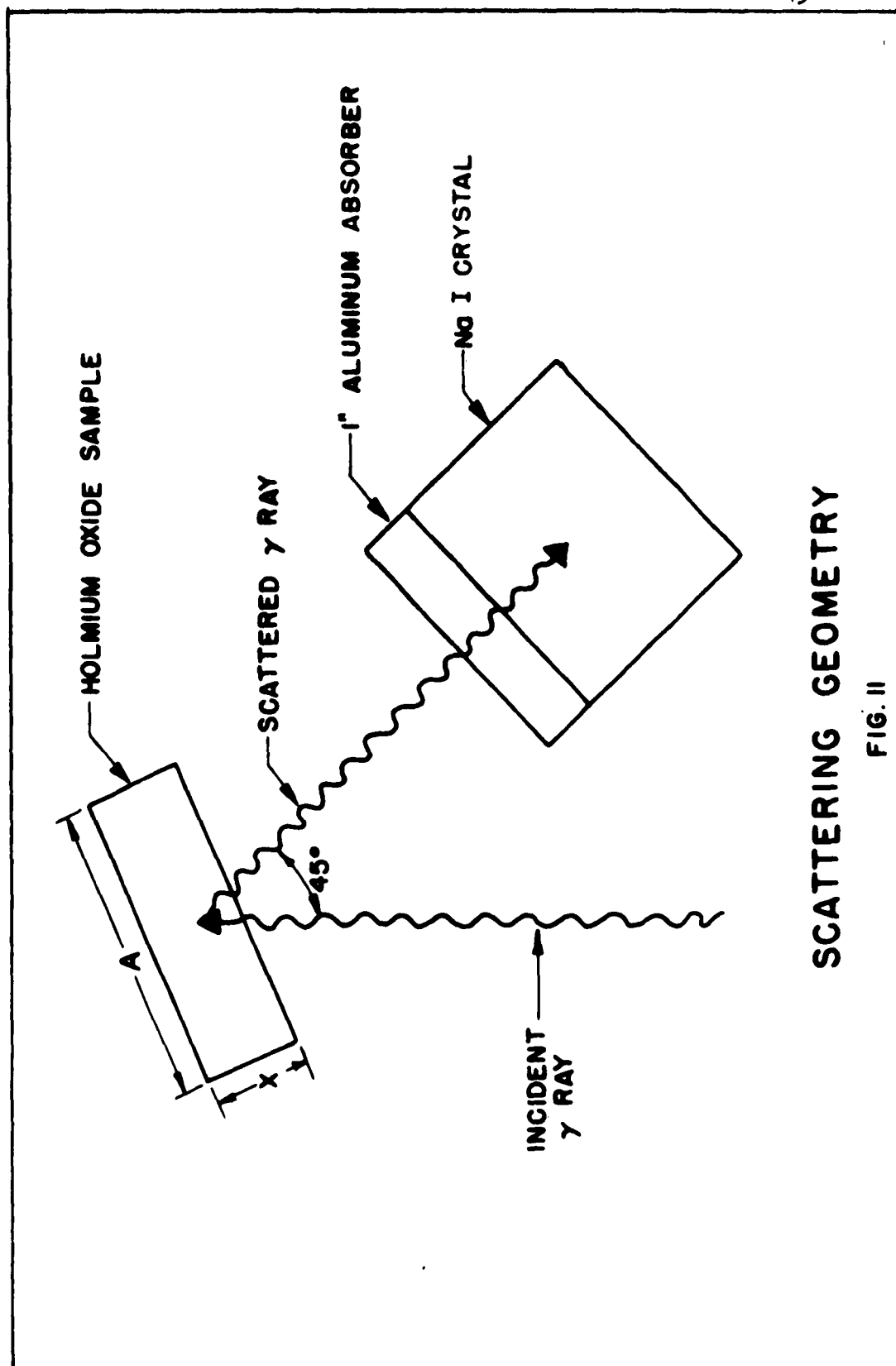
SCATTERING GEOMETRY

FIG. II

of a gamma ray striking the projected area of dA at the face of the sample,

(3) of the transmission, T_{in}, of the gamma ray to the depth x of the element,

(4) the number of nuclei per unit area, $N_0 \dfrac{dx}{\overline{d\sigma} \cos 22.5°}$, in the element,

(5) the differential cross section, $\dfrac{\overline{d\sigma}}{d\Omega}$, averaged over the angle subtended by

the crystal, (6) the transmission, T_0, of the gamma rays to the detector,

(7) the solid angle, Ω, subtended by the crystal face at the sample element,

(8) the fraction, F_i, of those gamma rays hitting the crystal which interact

with the crystal, (9) the fraction of interactions, F_p, which produce pulse

heights in the bin considered in determining the number of true coincidences,

and (10) the efficiency, F_e, of the electronic circuits. The total number of

true coincidences detected is the sum of the contributions of each element

of the sample, thus

$$N_t = \sum_v N_e P_\gamma \; T_{in} \; N_0 \; \frac{dx}{\cos 22.5°} \; \frac{\overline{d\sigma}}{d\Omega} \; T_0 \; \Omega \; F_i \; F_p \; F_e \qquad (25)$$

where $\sum_v$ denotes a sum over the volume elements.

This expression can be simplified by noticing that only T_{in}, T_0,

and Ω depend upon the depth, x, of the volume element. (The slight

dependence of F_i, and F_p on the depth can certainly be ignored.) If the

average depth, $\bar{x}$, is defined by

$$\Omega(\bar{x}) = \frac{\int \Omega(x) T_{in} T_0 \, dx}{\int T_{in} T_0 \, dx} \qquad (26)$$

and the effective number of nuclei per unit area is defined as

$$N_{0\,eff} = N_0 \int T_{in} T_0 \frac{dx}{\cos 22.5°} \qquad (27)$$

Eq. (25) can be written

$$N_t = N_e \frac{d\sigma}{d\Omega} F_e N_{0\ eff} \sum_A P_\gamma \Omega(\bar{x}) F_i F_p \tag{28}$$

where $\sum\limits_A$ denotes a sum over area elements at depth, $\bar{x}$, in the sample.

The average depth, which is easily calculated for a point source on the crystal axis, is about 0.8% less than 1/2 the sample thickness.

For elements on the crystal axis, the mean scattering angle is 135°. If the angular dependence of $\frac{d\sigma}{d\Omega}$ is $a + b\cos^2\theta$, then $\frac{\overline{d\sigma}}{d\Omega} = \frac{d\sigma}{d\Omega}(135°)$ All elements off the axis can be combined in pairs and averaged about 135°. Therefore $\frac{\overline{d\sigma}}{d\Omega}$ has been removed from the sum, and the bar omitted.

In the bremsstrahlung measurements, the number of detected true coincidences is

$$N_{tb} = N_{eb} P_{\gamma\ b} F_{ib} F_{pb} F_{eb} \tag{29}$$

where $P_{\gamma\ b}$ is the probability per detected electron of a gamma ray hitting the crystal in the bremsstrahlung position. It is also the probability of the gamma ray hitting the sample during a scattering run (due to the gamma ray collimator), i.e., $P_{\gamma\ b} = \sum\limits_A P_\gamma$. Combining Eqs. (28) and (29), the cross section can be written

$$\frac{d\sigma}{d\Omega} = \frac{N_t}{N_{\gamma\ eff}} \frac{F_{eb}}{F_e} \frac{1}{N_{0\ eff}} \frac{1}{\Omega_d} \tag{30}$$

where the effective number of incident gamma rays, $N_{\gamma\ eff}$, and the effective solid angle Ω_d are defined by

$$N_{\gamma\,eff} = N_e \frac{N_{tb}}{N_{eb}} \tag{31}$$

$$\Omega_d = \sum_A \frac{P_\gamma}{P_{\gamma b}} \frac{F_i}{F_{ib}} \frac{F_p}{F_{pb}} \overline{\Omega(x)} = C\,\Omega_p \tag{32}$$

and Ω_p is the geometric point source solid angle subtended by the crystal face at the center of the sample. C is less than one for two reasons: (1) the sample has finite extension, and (2) the edge effects of the crystal are more important in the scattering measurement (where the gamma ray beam is diverging as it strikes the crystal) than in the bremsstrahlung measurement (where the gamma ray beam is nearly parallel to the crystal axis). $\frac{N_{tb}}{N_{eb}}$ is the bremsstrahlung efficiency discussed in Section E of this chapter.

In order to insure that the electronic efficiencies were the same in the bremsstrahlung and scattering runs, the photopeak pulse heights were kept the same by adjusting the gamma ray detector high voltage to compensate for the slight gain shift due to the S magnet fringe field when the detector was in the scattering position. In addition, the electron and photon counting rates were kept low enough so that the electronic circuits would perform reliably independent of the rates. Then

$$F_{eb}/F_e = 1. \tag{33}$$

The effective number of nuclei per unit area was

$$N_{0\,eff} = N_0 \int_0^{X_0} e^{-\alpha X} \frac{dx}{\cos 22.5^o} = \frac{N_0}{\cos 22.5^o} \frac{1}{\alpha} (1-e^{-\alpha X_0}) \tag{34}$$

where $\alpha = \dfrac{2}{\cos 22.5^\circ}$ ($\mu_H \rho_H + \mu_0 \rho_0$) .. X_0 is the sample thickness,

and μ and ρ are the absorption coefficients and densities of the holmium and oxygen in the H_2O_3 sample.

The atomic absorption coefficients were obtained from the tables of G. W. Grodstein[39] (it was necessary to extrapolate from the coefficients given to the coefficient for $Z = 67$ for holmium), and the nuclear absorption for holmium was calculated assuming a cross section of 0.4 barns. The nuclear absorption by the oxygen was negligible. At 15 Mev, $N_{0\,eff}$ was 1.63×10^{22} nuclei/cm^2. This was 73% of the actual number of nuclei per unit area assuming no attenuation. A 3% error in the absorption coefficient would produce a 1% error in $N_{0\,eff}$. The variation in $N_{0\,eff}$ due to the energy dependence of the atomic absorption coefficients was about 3% from 11 Mev to 18 Mev.

In the remainder of this section, the calculation of the effective solid angle, Ω_d, will be described. For a point source on the crystal axis, 20.16 cm from the crystal face (this was the distance from the crystal face to the average depth in the sample as defined by Eq. (26)), the geometric solid angle, Ω_p, is 0.290 steradians. The correction factor, C, will be shown to be 0.69.

The effective solid angle was calculated assuming that the sample normal was parallel to the crystal axis. For each point of the sample closer to the crystal by dR due to the sample inclination there is a point an equal distance dR further from the crystal; therefore, to first order in dR/R, the solid angle averaged over the area of the sample is independent of the inclination. If P_γ has horizontal symmetry about the sample center (i.e., the sample is symmetrically illuminated), Ω_d will depend on the inclination only in terms of the order $(dR/R)^2$. For the

inclination of 22.5° at a point half way between the center and edge of the sample, $(dR/R)^2$ is about 0.4%. Crude tests in the bremsstrahlung position show that the sample illumination was horizontally symmetric. As was pointed out in Section E of this chapter, the fact that the bremsstrahlung efficiency was a maximum as a function of the beam position on the converter also indicates that the sample was symmetrically illuminated.

The average solid angle, $\bar{\Omega}(\mathbf{k})$, the interaction efficiency, F_i, and the energy loss spectrum were determined at 15.1 Mev and 12 Mev for uniformily illuminated disc sources of radii 0.5 in., 1.5 in., and 2.5 in. at a distance of 8 in. from the crystal by the Monte Carlo calculations of Miller and Snow.[40,41] In addition, the interaction efficiency and energy loss spectrum were calculated for broad parallel beams of radii 2 in. and 2.5 in. incident on the crystal. The pulse height spectra were determined by smearing the energy loss spectra with a Gaussian resolution function to give pulse height spectra similar to those obtained in the bremsstrahlung measurements. The pulse height bin considered in determining the number of true coincidences was the group of 5 channels in the photopeak of the pulse height spectrum. In Fig. 7, these 5 channels contain the fraction of the total counts equal to the fraction of the total area which is under the photopeak (defined by the half maximum points). Thus F_p is the fraction of the area under the photopeak. The salient features of the results of these calculations will now be discussed. The statistical accuracy of the calculations (5000 histories were taken for each case) was 1% or less for each case.

1. The resolution was the same for all the disc sources and the broad parallel beam sources. This was because the 25% resolution function essentially determined the resolution.

2. The product of $F_i F_p \Omega(\bar{x})$ for the smallest and largest discs differed by only 4%, thus an elaborate scheme for choosing area elements to evaluate Ω_d was not necessary.

3. The product $F_{ib} F_{pb}$ for the broad parallel beams of 2 in. and 2.5 in. radii differed by only 0.7%, which was about the uncertainty in the calculation.

4. The ratio $F_i F_p \Omega(\bar{x})/F_{ib} F_{pb}$ was 1% higher at 15 Mev than at 12 Mev. (The product $F_i F_p \Omega(\bar{x})$ was only 1.4% higher at 15 Mev than at 12 Mev.)

5. Figure 12 shows the calculated pulse height spectrum at 15 Mev for a 2.5 in. disc source (heavy line) and a broad parallel beam (dashed line). It can be seen that the low pulse height plateau for these spectra is smaller than the experimental spectrum (Fig. 7). At least part of this difference is due to the 1 in. thick aluminum plate on the fact of the crystal which was neglected in the calculations. The absorption and Compton scattering of the gamma ray beam in this plate was not considered since the ratio $F_i F_p/F_{ib} F_{pb}$ should not be affected, in first order.

The sum in Eq. (32) was approximated using three uniformly illuminated area elements: a disc source of radius 0.5 in., the annular ring between $r_1 = 0.5$ in. and $r_2 = 1.5$ in., and the annular ring between $r_2 = 1.5$ in, and $r_3 = 2.5$ in. The relative illumination for each area element, $P_r/P_{r b}$, was estimated using the angular distribution curves of J. Miller[37] discussed in Section E, giving 3% for the first area, 45% for the second, and 52% for the third. (If the entire sample had been uniformly illuminated, the ratios would have been 5%, 19%, and 76%.)

DISC SOURCE AT 8"

BROAD PARALLEL BEAM

PULSE HEIGHT (ARBITRARY UNIT)

CALCULATED PULSE HEIGHT SPECTRA

FIG. 12

RELATIVE NUMBER OF PULSES
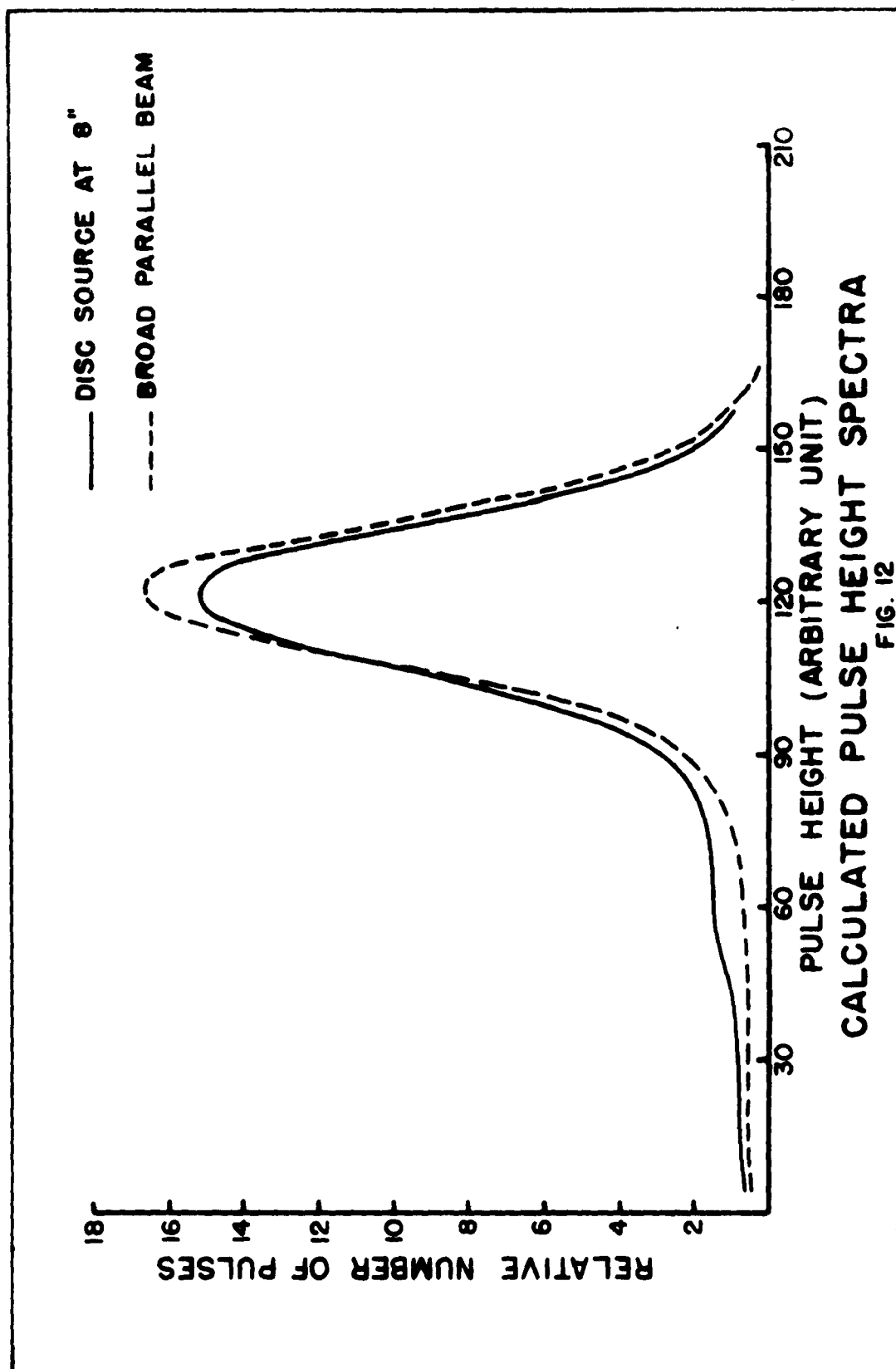
This approximation for the sum, and the results of the Miller and Snow calculations gave for the value of the effective solid angle,

$$\Omega_d = 0.200 \pm 0.004 \text{ steradian}$$

or

$$\Omega_d = 0.69 \, \Omega_p$$

This result is the same (within 0.5%) as that obtained by approximating the sample by one uniformly illuminated disc of radius 1.5 in. It is interesting to examine in more detail the correction factor, C. For a uniformly illuminated disc source, this factor is,

$$C = \frac{\Omega(\bar{x})}{\Omega_p} \qquad \frac{F_i}{F_{ib}} \qquad \frac{F_p}{F_{pb}} \tag{35}$$

The Miller and Snow calculations gave for the 1.5 in. disc, 0.97 for the ratio of the average solid angle to the point source solid angle, $\frac{\Omega(\bar{x})}{\Omega_p}$; 0.76 for the interaction correction, F_i/F_{ib}; and 0.93 for the photopeak fraction correction, F_p/F_{pb}.

Most of the holmium scattering data were taken using the geometry shown in Fig. 11; however, for some of the data, the crystal was 9 in. from the sample center and collimated to a diameter of 4 in. (See Table I; the crystal to sample distance was changed to 8 in. on May 18.) The normalization factor, K, needed to compare these two sets of data is just the ratio of the effective solid angles for the two geometries. An estimate of this ratio can be obtained from the results of the calculations discussed above. For the case of the collimated crystal at 9 in., the corrections due to the edge effects of the crystal should be small, i.e., $(F_i/F_{ib})(F_p/F_{pb}) \approx 1$. Then C is about 0.97, and the effective solid

angle is $(\Omega_d)_{9\ in.} = 1.48$ steradians. Thus the normalization factor, K, is about 1.35. An attempt was made to measure K using a carbon sample. The result was 1.22 ± 0.10. This result seems unreasonably low since a lower limit estimate gives 1.25 for the ratio of the point source solid angles if the crystal were collimated in both cases.

H. Background

The background due to the main electron beam which loses only a very small amount of energy in the converter was considerably reduced by stopping this beam in a paraffin beam stopper right at the exit of the spectrometer. With this arrangement, the gamma ray detector could be placed with its axis in the horizontal plane. Since most of the runs were taken with the dispersions of the D and S magnets matched (therefore the ratio of the magnetic fields was approximately constant), the position of this beam did not change with E . This simplified the shielding problem. Figure 13 shows the spectra of single gamma rays detected for 8×10^6 electrons with no sample, a carbon sample, and the holmium sample. Notice that the 15.1 Mev gamma rays scattered from carbon are clearly evident in the region of channels 59 to 63. Furthermore, when holmium is the sample, only a very small fraction of the gamma rays do not come from the sample.
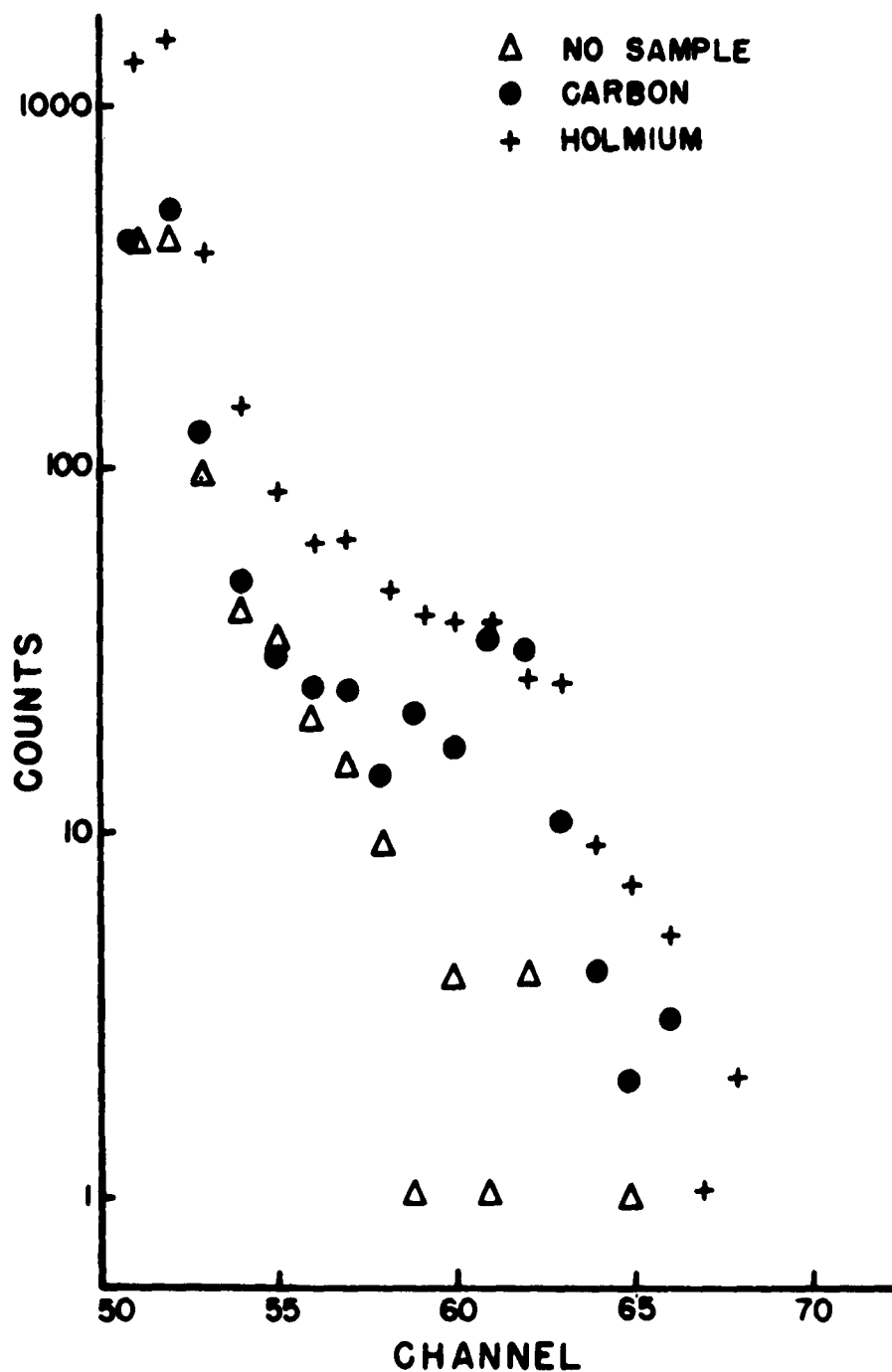
SINGLES SPECTRA
WITH DIFFERENT SAMPLES
FIG. 13

CHAPTER IV

EXPERIMENTAL PROCEDURE

A. Determination of Background

The differential scattering cross section is given by Eqs. (30) and (33),

$$\frac{d\sigma}{d\Omega} = \frac{N_t}{N_{\gamma \, eff}} \cdot \frac{1}{N_{0 \, eff}} \cdot \frac{1}{\Omega_d} \tag{36}$$

The number of true coincidences, N_t, is the difference between the total number of coincidences, N_{tot}, and the number of chance coincidences, N_{ch}. The scattering from the oxygen in the sample and from the aluminum foil container was negligible.[4] The effective number of incident gamma rays, $N_{\gamma \, eff}$, is the number of detected electrons, N_e, times the bremsstrahlung efficiency, N_{tb}/N_{eb}. The determination of N_{tb}/N_{eb}, $N_{0 \, eff}$, and Ω_d has been discussed in the preceding chapter. N_{tot} and N_e are measured directly. In this section, the experimental determination of N_{ch} will be described.

The number of chance coincidences per pulse is the product of the fraction of the time the coincidence circuit is sensitized by the electrons, and the number of gamma ray pulses large enough to activate the coincidence circuit. If the instantaneous rates of singles electrons and gamma rays were known, the number of chance coincidences per pulse could be calculated from

$$n_{ch} = \frac{2\mathcal{T}}{T} \, n_e \, n_s \tag{37}$$

where $2\mathcal{T}$ is the coincidence resolving time, T is the pulse duration, and n_e and n_s are the numbers of electrons and gamma rays per pulse. Since both n_e and n_s are proportional to the beam intensity, the chance

rate is proportional to the square of the beam intensity. Thus N_{ch} cannot be calculated from the average electron and gamma ray rates if there are any fluctuations in the beam intensity. N_{ch} can be obtained using the "singles rejection ratio," R, which is defined as the average chance coincidence rate divided by the average single gamma ray pulse rate. If N_s is the total number of single gamma ray pulses for a given run, then $N_{ch} = R\,N_s$. (The chance spectrum has the same shape as the singles spectrum unless the number of truly coincident gamma rays is an appreciable fraction of all the gamma rays hitting the crystal as is the case when 15.1 Mev gamma rays are scattered by C^{12}. A gamma ray which makes a true coincidence with an electron from one electron detector cannot make an accidental coincidence with an electron from another detector because all such double coincidences are rejected by the electronics.) The singles spectrum can be recorded by successively biasing the electron side of each coincidence circuit so that gamma ray pulses can activate the following discriminator whether or not electron pulses arrive simultaneously. (The singles spectra produced by the four coincidence circuits vary slightly due to the electronics used to separate the 100 channel analyzer into four 25 channel groups.)

There are two ways to determine R experimentally. During a scattering run, the fourth coincidence circuit records only chance coincidences because the cable delays are adjusted so that pulses from truly coincident events do not arrive at the coincidence circuit simultaneously. (The number of chance coincidences in the pulse height region of interest for the other three circuits could be obtained from the measured number in the fourth coincidence circuit after correcting for the difference in the circuits; however, since the number of chance coincidences is necessarily kept small, a direct determination would have a large statistical uncertainty.)

It is more accurate to obtain R from the singles measurement and the large number of low energy chance gamma rays in each group. The value of R determined in this way can be used to calculate N_{ch} with the aid of the known number of singles in the pulse height region of interest. The fourth coincidence circuit is used to check this system, and to detect anomalies which might arise due to some malfunction of the other electronic circuits.

B. Procedure for Taking Data

For each desired value of E_γ , the desired Hall voltages, V_D and V_S, were determined from the calibration curves for $E_b = 1.3\ E_\gamma$, and $E_e = 0.3\ E_\gamma$. (Thus E_b/E_e was set at 4.3 which is very nearly equal to the dispersion matching ratio.) The S and D magnets were adjusted to give the magnetic fields which produced the required Hall effects. The betatron energy was set approximately equal to E_b, and the orbit expansion system was adjusted so that the beam was extracted in a 300 microsecond pulse, centered about the peak betatron amplitude (i.e., the beam pulse was symmetric about the maximum energy of the betatron cycle.) The beam was then focused at F_1 of Fig. 1 by adjusting the quadrupole magnet current while observing the beam on a scintillating screen inserted at F_1 for this purpose. When this screen was removed, fine adjustments were made in the betatron energy to position the beam on the converter so that the high energy edge of the beam coincided with the high energy edge of the converter.

The bremsstrahlung efficiency was then measured after reducing the injector filament current until the electron scaler counted only about 10 electrons per second. (This corresponded to a reduction of the yield by about 2×10^4.) The gamma ray detector, which was mounted on a cart that rolled in a fixed circle around the sample position, was then placed

in the reduced bremsstrahlung beam. The gain of the gamma detector was adjusted so that the pulse height of the photopeak was a fixed size independent of E_γ. This was done so that the resolving time and the cable delay of the electron and gamma ray sides of the coincidence circuit would be independent of E_γ. A few points on the cable curve (see Fig. 6) were taken to check that the cable delay was adjusted properly.

The efficiency was then recorded as in Fig. 5. After the efficiency measurement had been completed, the gain of the gamma ray detector was calibrated by using the 1.33 Mev gamma rays from radioactive Co^{60}. The last dynode pulses from the gamma ray photomultiplier were amplified (with an auxiliary stable amplifier), and displayed in the 100 channel analyzer. The position of the photopeak of the 1.33 Mev gamma rays was recorded for future reference during the run. The gamma ray detector was then rolled into the 135° scattering position. To maintain the gain, the high voltage of the photomultiplier had to be increased by about 20 volts out of 2500 volts because the counter was now closer to the fringe field of the S magnet. The betatron yield was then increased, and the beam position on the converter was checked. If for any reason the beam position had changed, the efficiency was measured again.

With the yield increased to about 1.6×10^{4} electrons per second in the center electron detector, singles runs were taken with and without the sample in place. Following this, a series of one hour scattering runs was taken. After about 10 such runs, the bremsstrahlung efficiency was again checked, and a new E_γ was chosen.

In order to minimize the number of chance coincidences, while maintaining a high average counting rate, the electron counting rate was kept as steady as possible. The beam position and the fields of the spectrometer and dispersion magnets were monitored periodically during

the runs. The gain of the gamma detector was checked about every three hours. The gain was readjusted if the position of the photopeak of the 1.33 Mev Co^{60} gamma rays changed by as much as two channels in 40. Singles spectra were taken after every four or five coincidence runs.

Two additional measurements were taken as checks on the reliability of the data. Because the NaI crystal is so close to the main photon beam, scattering runs were taken from time to time with no sample in order to be certain that all true coincidences came from the sample. Scattering runs were also taken with the sample in place but the gamma ray delayed by enough extra cable so that all the coincidence circuits recorded only chance coincidences. The chance spectrum of each circuit was then compared with the corresponding singles spectrum, and the variation of singles rejection ratios from one circuit to another due to different resolving times could be determined. This measurement showed that each chance spectrum was identical in shape to its corresponding singles spectrum, and that the singles rejection ratio was the same for each circuit.

C. Analysis of the Data

The singles rejection ratio is most easily determined graphically. Semilog plots are made of the singles and chance spectra. The vertical shift required to overlay the chance spectrum on the singles spectrum gives the singles rejection ratio times the ratio of electrons used to obtain the spectra. Figure 14 shows the semilog plots of a singles run and chance coincidence run at 12.49 Mev. The abscissa is the channel number of the 100 channel analyzer. (Channels 75 to 100 displayed the coincident gamma ray pulses from the fourth coincidence circuit used for chances. The gain had been adjusted to place the photopeak for $E_\gamma = 12.49$ Mev in channel 90.) The curve is sketched from the singles points which were
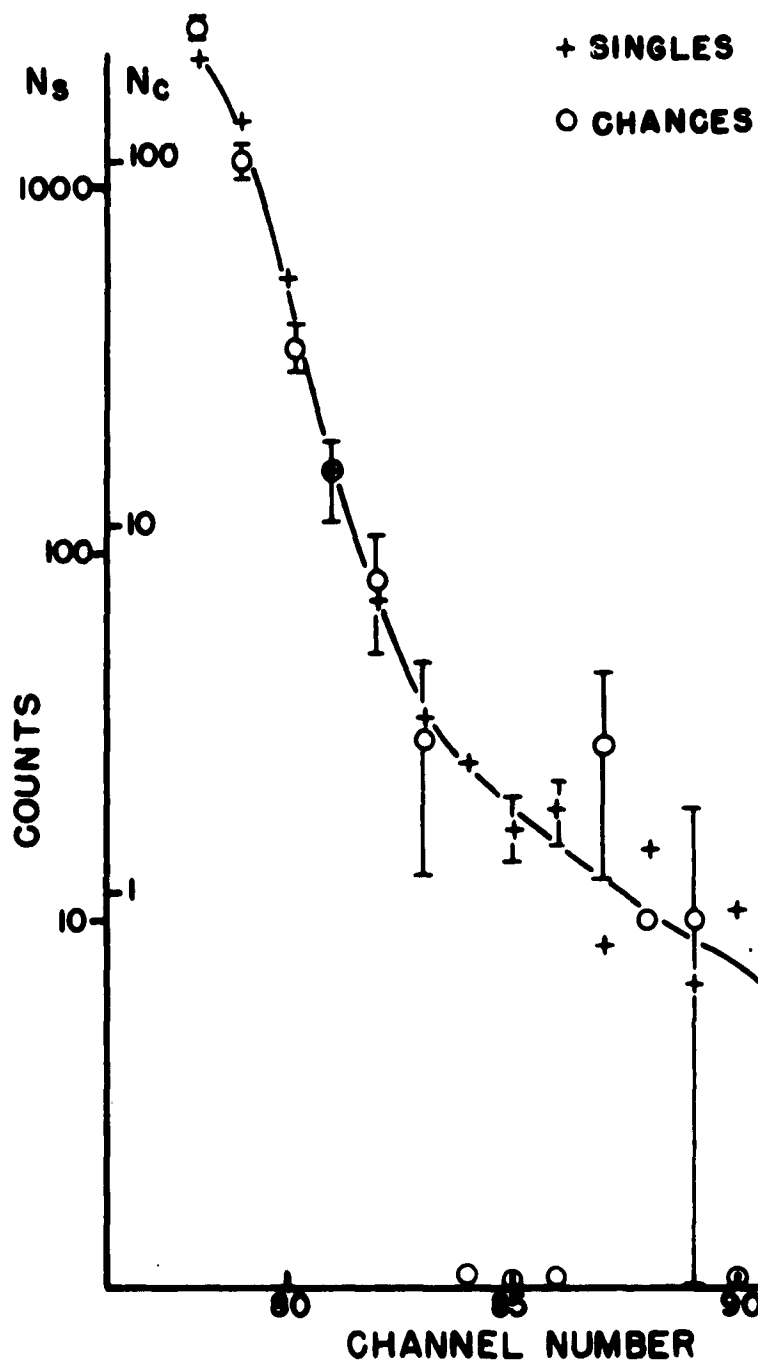
CHANCE COINCIDENCE SPECTRUM

FIG. 14

taken for 8×10^6 electrons in about 8 minutes. The circles represent the chance coincidences collected in 3 one-hour runs for 1.8×10^8 electrons. From the vertical axes for N_s and N_{ch}, the singles rejection ratio is:

$$R = \frac{N_s/\text{electron}}{N_{ch}/\text{electron}} = \frac{85/1.8 \times 10^8}{1000/8 \times 10^6} = \frac{1}{265} \qquad (38)$$

Once this normalization factor was determined for a run or set of runs, the chance coincidence curves could be drawn for the coincidence spectra of the other three coincidence circuits. Figure 15 shows the semilog plot of all coincident gamma rays associated with the middle electron detector for the same 3 hours as Fig. 14. The curve which represents chance coincidences is sketched from the singles points (not shown in Fig. 15) as in Fig. 14. Because of the steepness of the chance curve, and the large number of chances in the low channels, only 5 channels in the photopeak were accepted for determining both the bremsstrahlung efficiency and the number, N_t, of true coincidences. For example, in Fig. 15 there are 24 total counts in the channels 63 to 67; the expected number of chances, obtained from the curve, is 4.2. Assuming that the uncertainty in the chance number determined in this way is negligible, the number of true counts is $19.8 \pm \sqrt{24}$. The corresponding value in the chance coincidence group can be obtained from Fig. 14; there are three counts in the channels 88 to 92, while the singles curve implies 3.1 chances. The number $N_{tot} - N_{ch} = -0.1 \pm 1.73$ should, of course, always be zero within statistics.

The chance coincidence background subtraction was determined in this way for all the scattering data. If the electron rates were the same, and there were no shifts in the electronics, 2 or 3 one-hour runs were
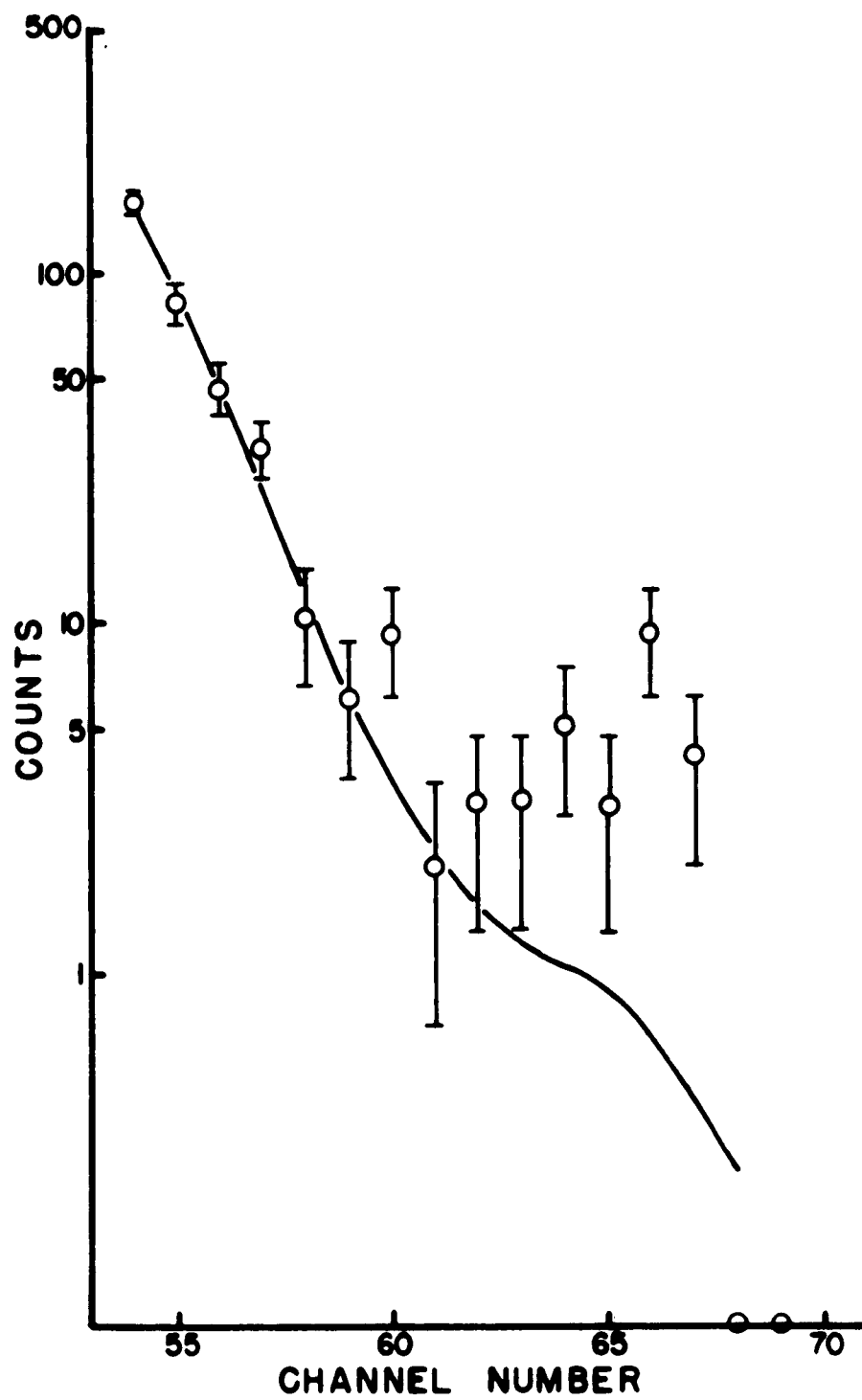
SPECTRUM OF ALL COINCIDENCES

FIG. 15

added as in the example above; the most recent singles run was used to determine the chance rate. The number of true coincidences in each channel was then determined from all the scattering runs at the same E_γ . The five channels in the photopeak were chosen from the bremsstrahlung efficiency measurement allowing ± 1 channel shifts due to electronic shifts or gain shifts as indicated by the scattering data. In Fig. 16 the number of true coincidences in each channel for 19 hours and 1.27×10^9 electrons is plotted versus channel number for the middle detector at 12.49 Mev. The curve, whose shape was obtained from the bremsstrahlung measurement, shows that the true coincident pulses produced the same pulse height distribution as did the monochromatic gamma rays selected during the corresponding bremsstrahlung measurement.
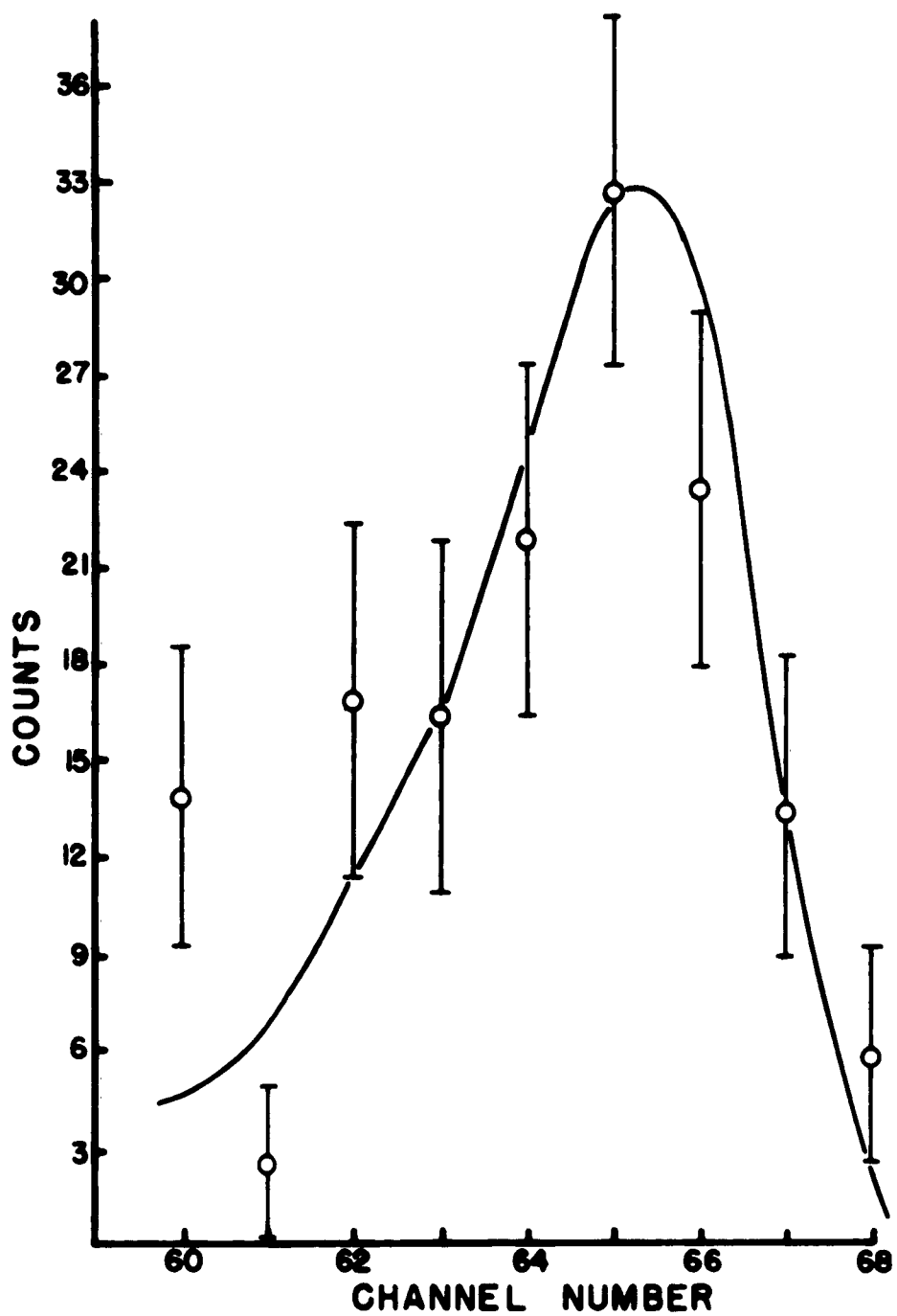
SPECTRUM OF TRUE COINCIDENCES

FIG. 16

CHAPTER V

RESULTS AND CONCLUSIONS

A. Results

The data are arranged in Table II in order of increasing E_γ

(column 1); three data points and one chance channel were obtained

simultaneously. The corresponding S and D magnet settings, and dates

appeared earlier in Table I. Column 2 gives the value of Ω_d in accordance

with the geometry used; Ω_d was 0.200 steradians for the uncollimated

crystal at 8 in. from the sample center, while Ω_d was 0.148 steradians

for the collimated crystal at 9 in. Column 3 gives the effective number of

incident gamma rays, defined as $N_{\gamma\,eff} = N_e\,N_{tb}/N_{eb}$. N_{tb}/N_{eb} was deter-

mined to about 3% during the typical bremsstrahlung efficiency run. (The

efficiency for the chance coincidence group was not measured for each

energy. When measured it was found to be nearly equal to the efficiency

of the highest energy group, therefore $N_{\gamma\,eff}$ is taken to be the same for

these two groups. The efficiency of the chance group is not used in the

determination of either the cross section or the chance number.) The total

number of coincidence counts, N_{tot}, is given in column 4, and the calculated

number of chance counts, N_{ch}, is given in column 5. The differential cross

section, calculated from Eq. (36) is given in column 6. In column 7, the

data from the three electron detectors are combined to improve the statistics

at the expense of the energy resolution. The errors assigned in columns 6

and 7 are statistical. At E_γ around 15 and 15.5 Mev, data were taken with

both geometries. For these energies, the cross sections calculated from the

combined data are also given. In Fig. 17, the differential scattering cross

TABLE II

EXPERIMENTAL RESULTS

E_γ Mev	Ω_d Sterad	$N_{\gamma\,eff}$ $10^7\,x$	N_{tot}	N_{ch}	$\dfrac{d\sigma}{d\Omega}$ $10^{-28}\,\dfrac{cm^2}{sterad}$	$\dfrac{d\sigma}{d\Omega}$ av $10^{-28}\,\dfrac{cm^2}{sterad}$
10.91	0.148	4.00	20	14.9	0.52 ± 0.46	
11.00		4.16	17	18.3	- 0.12 ± 0.45	0.57 ± 0.28
11.09		3.55	23	10.3	1.45 ± 0.54	
Chance		3.55	08	12.1		
11.63	0.148	9.23	89	42.3	2.05 ± 0.42	
11.73		9.19	100	41.0	2.60 ± 0.44	2.35 ± 0.20
11.83		8.31	91	41.6	2.41 ± 0.47	
Chance		8.31	35	31.3		
11.89	0.200	6.10	96	32.4	3.14 ± 0.49	
11.99		6.90	111	40.2	3.15 ± 0.47	3.20 ± 0.28
12.09		7.07	115	37.3	3.31 ± 0.46	
Chance		7.07	26	35.0		
12.39	0.148	10.77	121	51.6	2.62 ± 0.48	
12.49		10.63	159	49.5	4.19 ± 0.49	3.47 ± 0.27
12.59		9.55	137	51.7	3.62 ± 0.50	
Chance		9.55	40	45.1		
12.90	0.200	5.40	95	40.8	3.03 ± 0.52	
13.01		6.15	107	39.0	3.34 ± 0.51	2.87 ± 0.28
13.12		6.15	87	40.9	2.29 ± 0.46	
Chance		6.15	35	28.0		
13.39	0.148	6.08	67	33.5	2.25 ± 0.56*	
13.50		5.98	70	29.5	2.76 ± 0.57*	2.75 ± 0.34*
13.61		5.68	69	23.1	3.30 ± 0.64*	
Chance		5.68	20	24.2		
13.90	0.200	5.18	96	40.7	3.25 ± 0.58	
14.01		6.39	104	41.6	2.97 ± 0.48	3.11 ± 0.30
14.12		6.33	105	42.8	3.03 ± 0.50	
Chance		6.33	23	27.1		
14.38	0.148	9.56	96	41.5	2.34 ± 0.43	
14.50		9.33	122	33.9	3.88 ± 0.50	2.98 ± 0.28
14.62		8.79	95	36.9	2.73 ± 0.46	
Chance		8.79	34	33.0		

TABLE II--<u>Continued</u>

E_γ Mev	Ω_d Sterad	N_γ eff 10^7 x	N_{tot}	N_{ch}	$\dfrac{d\sigma}{d\Omega}$ $10^{-28}\dfrac{cm^2}{sterad}$	$\dfrac{d\sigma}{d\Omega}$ av $10^{-28}\dfrac{cm^2}{sterad}$
15.00	0.200	2.83	48	18.3	3.21 ± 0.75	
15.12		2.99	62	18.9	4.42 ± 0.75	3.97 ± 0.46
15.24		3.14	67	23.6	4.22 ± 0.80	
Chance		3.14	26	22.0		
15.00	0.148	3.65	45	20.8	2.73 ± 0.76	
15.12		3.85	61	22.2	4.16 ± 0.74	3.31 ± 0.46
15.24		4.04	55	25.4	3.02 ± 0.76	
Chance		4.04	20	18.5		
15.34	0.200	5.51	115	35.9	4.40 ± 0.60	
15.46		6.57	110	31.2	3.68 ± 0.49	3.88 ± 0.30
15.58		6.12	109	36.2	3.64 ± 0.53	
Chance		6.12	32	31.2		
15.34	0.148	12.70	186	64.0	3.97 ± 0.44	
15.46		13.00	176	55.5	3.82 ± 0.42	4.08 ± 0.26
15.58		11.30	173	49.9	4.50 ± 0.37	
Chance		11.30	34	34.3		
15.85	0.200	9.91	183	67.3	3.59 ± 0.42	
15.98		12.20	238	70.9	4.21 ± 0.39	3.84 ± 0.23
16.11		12.20	210	64.4	3.68 ± 0.37	
Chance		12.20	57	59.7		
16.37	0.200	5.12	93	35.3	3.45 ± 0.59	
16.50		6.23	110	31.1	3.90 ± 0.52	4.46 ± 0.32
16.63		6.51	155	32.4	5.80 ± 0.59	
Chance		6.51	18	29.4		
16.85	0.200	8.32	180	55.9	4.61 ± 0.51	
16.99		10.60	211	61.4	4.36 ± 0.42	4.21 ± 0.26
17.13		10.60	187	56.0	3.76 ± 0.30	
Chance		10.60	39	43.2		
17.77	0.200	3.57	79	33.3	3.99 ± 0.76	
17.92		4.08	62	26.6	2.72 ± 0.60	3.42 ± 0.41
18.07		3.82	80	35.8	3.61 ± 0.73	
Chance		3.82	21	27.3		

TABLE II--Continued

E_γ Mev	Ω_d Sterad	N_γ eff 10^7 x	N_{tot}	N_{ch}	$\dfrac{d\sigma}{d\Omega}$ $10^{-28}\dfrac{cm^2}{sterad}$	$\dfrac{d\sigma}{d\Omega}$ av $10^{-28}\dfrac{cm^2}{sterad}$
18.06	0.148	4.18	45	11.4	3.38 ± 0.68	
18.21		4.39	43	12.6	2.91 ± 0.60	3.23 ± 0.39
18.36		4.14	47	13.3	3.42 ± 0.74	
Chance		4.14	8	11.8		
18.75	0.200	8.69	115	67.2	1.72 ± 0.41/	
18.90		8.44	179	92.1	3.22 ± 0.48/	2.64 ± 0.28/
19.05		9.05	179	92.3	2.98 ± 0.45/	
Chance		9.05	40	45.6		
15.00	average				2.94 ± 0.53	
15.12					4.27 ± 0.65	3.60 ± 0.30
15.24					3.54 ± 0.49	
15.34	average				4.10 ± 0.19	
15.46					3.77 ± 0.33	4.01 ± 0.19
15.58					4.20 ± 0.34	
07.94	0.200	1.08	7	10.3	0	
08.01		1.47	22	18.4	0.81 ± 0.92	0.00
08.08		1.33	23	23.4	0	
Chance		1.33	14	13.1		
07.02	0.200	0.45	5	.5.2	0	
07.08		0.61	7	3.9	1.6 ± 1.8	0.55 ± 1.1
07.14		0.55	3	4.0	0	
Chance		0.55	2	1.5		

*There is an additional 5% uncertainty for these runs because of anomalies in the determination of efficiency

/There is an additional 20% uncertainty for these runs because of anomalies in the determination of N_{ch} and the efficiency.
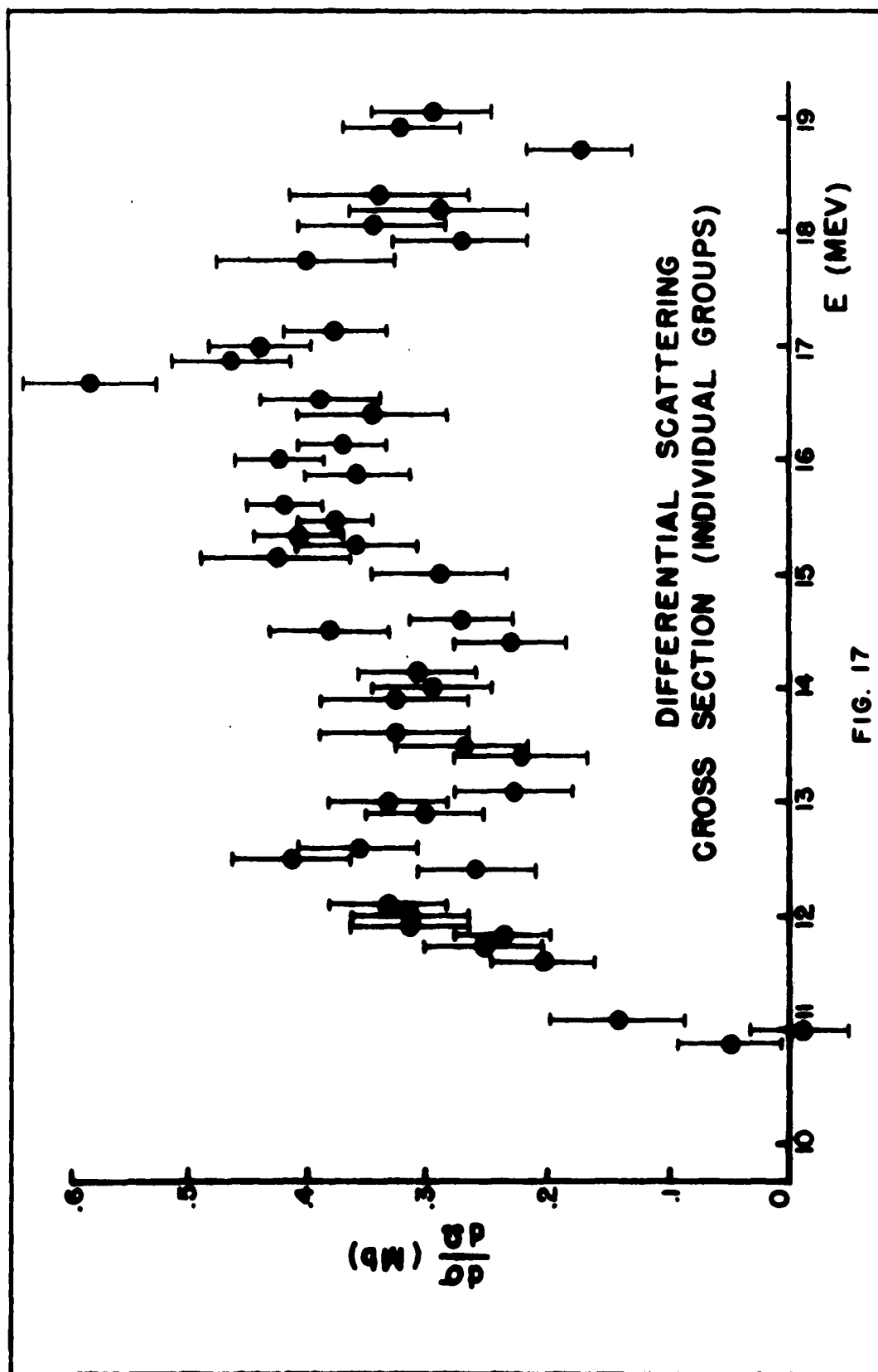
DIFFERENTIAL SCATTERING
CROSS SECTION (INDIVIDUAL GROUPS)

FIG. 17

section given in column 6 is plotted as a function of E_γ from E_γ = 10.91 Mev to E_γ = 19.05 Mev. The energy resolution for each point is about 0.6% as given in Chapter III, Section C.

B. Accuracy and Reliability of Data

In addition to the statistical uncertainties in the total number of coincidences, N_{tot}, used to determine the errors given in Table II, and shown in Fig. 17, there are uncertainties in the determination of the quantities Ω_d, N_e, N_{tb}/N_{eb}, and N_{ch} which lead to an uncertainty in the cross section. Possible errors in the determination of N_e and Ω_d will systematically affect all the data, therefore these will be discussed first.

The number of detected electrons, N_e, differs from the true number of secondary electrons from the converter hitting the electron detector because of (1) background pulses not associated with converter electrons, and (2) counting losses in the electron scalers. The background rate was measured periodically throughout the experiment by comparing the electron counting rates with, and without the converter in place. The background was always about 2% (or less) of N_e. (Much of this background was associated with the stopping of the main electron beam in the paraffin just outside the S magnet. The background may not be the same with, and without the converter in place because the main beam is scattered by the converter.) No correction was made for this background, however, because it was the same in both the bremsstrahlung and scattering runs; therefore, the effective number of gamma rays, $N_{\gamma\ eff}$ which is proportional to N_e/N_{eb} is not affected. The counting loss in the electron scaler was about 0.7% for the normal rate of 1.6×10^4 electrons per second in a scattering run. This does affect $N_{\gamma\ eff}$ because the loss is much less in the bremsstrahlung measurement where

the electron rate was only about 10 electrons per second. There was a similar loss in the number of true coincidences, N_t. Truly coincident gamma rays were lost if they also made chance coincidence with an electron from one of the other detectors, because all such double coincidences were rejected by the electronics. The fractional loss of true coincidences is the probability that a gamma ray will make an accidental coincidence in any of the other three circuits; this probability is 3R. For the typical singles rejection ratio of 1/265, this loss was 1.1%. Since the electron counting rate was about the same for all the runs (therefore R was also nearly constant), these two losses were about the same magnitude, and their effects on the cross section cancelled. If there were fluctuations in the rates, both losses would have been affected similarly.

The uncertainties in Ω_d (for the later data) are estimated to be: 2% due to the statistical uncertainty of the Monte Carlo calculation, 1% in the measurement of the distance, and 1% in the average over the sample. The maximum systematic error for these data is then 4% (assuming negligible uncertainty in N_e) while the probable (rms) error is 2.5%. The systematic error in the earlier data due to uncertainties in the effective solid angle is estimated to be less than 8% and probably about 4%.

The uncertainties in the bremsstrahlung efficiency, N_{tb}/N_{eb}, and the number of chance coincidences, N_{ch}, fluctuate from one run to another, and do not contribute to a systematic uncertainty in all the data. There are three kinds of uncertainties in the bremsstrahlung efficiency due to: (1) statistical error in the measurement of N_{tb}/N_{eb}, (2) insufficient monitoring of the beam to insure the same distribution of electrons on the converter in both the scattering and bremsstrahlung measurements, and (3) possible gain shifts which change the fraction of the pulses in the

photopeak which is defined by a fixed number of channels (five). The statistical error was about 3% for all the runs. The uncertainty due to insufficient monitoring was much larger in the earlier data ($\Omega_d = 0.148$) than in the later data ($\Omega_d = 0.200$) both because the monitoring was more difficult, and the efficiency was more sensitive to beam position as discussed in Section E of Chapter III. For the earlier runs the uncertainty due to insufficient monitoring is estimated to be about ± 6%. For the later data, the uncertainty is estimated to be about 2% almost entirely due to the difficulties in monitoring the beam position in the bremsstrahlung measurement. Since the normal position of the beam was one of maximum efficiency for these data, any error would tend to give too low an efficiency, and therefore too high a cross section. The uncertainty due to gain shifts is estimated to be ± 3%.

Since N_{ch} is calculated from the curve of singles gamma rays, measured with high statistical precision, there is negligible statistical uncertainty in this number; however, gain shifts in the gamma ray detector, and in the pedestals used to separate the 100 channel analyzer into four groups introduce uncertainties in the fitting of the coincidence spectra to the singles spectra. The uncertainties in N_{ch} are probably about 5% giving about 3% uncertainty in N_t. The root mean square estimate of the fluctuating uncertainties is thus ± 8% for the earlier data, and ± 5% for the later data. In addition, there is a probable 2% error tending to over-estimate the cross section in the later data.

In addition to these nominal systematic and fluctuating uncertainties, there are anomalies which increase the uncertainties in some of the data. There is an additional uncertainty of about 5% in the data at $E_\gamma = 13.5$ Mev because of difficulties in determining the bremsstrahlung efficiency. At

E_γ = 18.9 Mev, there is an additional uncertainty of about 20% because of difficulties in determining both N_{ch} and the bremsstrahlung efficiency.

Various checks have been made on the final data in order to detect possible systematic error, and to get a better understanding of the reliability of the results. As was mentioned in Chapter III, the relative bremsstrahlung efficiencies were examined, and the small fluctuations could all be attributed to statistical fluctuations (and the small bias changes that were made on May 18) except for a large (10%) fluctuation which occurred during the runs at E_γ around 18.9 Mev. An indication of the reliability of the method of background subtraction was obtained by comparing the total number of chance counts with the total calculated number for the chance group. The sum of $N_{tot} - N_{ch}$ was 568 - 608 = -40 ± 38, where the uncertainty is the rms value of the statistical error in N_{tot} and the 5% uncertainty in N_{ch} (estimated from the difficulty encountered in fitting the chance curves to the singles curves as discussed above). While this difference is only about one standard deviation from the expected value of 0, the possibility exists that N_{ch} has been slightly over estimated. A uniform decrease in N_{ch} of 5% would give about a 3% increase in the cross section data. There seem to be no anomalously large fluctuations in the relative values of N_{ch} for the three groups in coincidence except at E_γ around 18.9 Mev where N_{ch} is significantly smaller for the lowest energy group than for the other two groups. Because of this anomaly, and the anomalously large fluctuation in efficiency, there is an additional 20% uncertainty for these points as discussed above, and as indicated in Table II.

A final reliability check was the comparison of the cross section at each energy point with the average of the three points taken simultaneously to see if one of the coincidence circuits was, for some reason, giving anomalously high or low values of the cross section compared with the

other circuits. The sum of the deviations from the average was - 0.5 ± 0.3 mb for the lowest energy group, and + 0.25 ± 0.3 mb for the other two groups. Thus the lowest energy group seems to give a somewhat lower value for the cross section than the other two groups; however, the discrepancy is slight, and could easily be statistical. No correlation was found between a low (or high) cross section value for any of the individual groups and a low or high bremsstrahlung efficiency.

As a result of these accuracy estimates, and the reliability checks discussed above, the total uncertainties assigned to the data in addition to the statistical errors (and anomalies) given in Table II are:

1. Systematic error in either direction

    (a) Earlier data,   probable, ± 4%;   maximum, ± 8%

    (b) Later data,   probable, ± 2.5%;   maximum, ± 4%

2. Fluctuating errors in either direction (rms)

    (a) Earlier data, ± 8%

    (b) Later data, ± 5%

3. Errors in one direction only (rms)

    (a) Earlier data, + 3%

    (b) Later data, + 3.5%

    (These errors tend to underestimate the cross section.)

C. Conclusions

1. No Fine Structure

Figure 17 shows no evidence of fine structure. In about 75% of the cases, adjacent points are within a standard deviation of each other; only at 16.63 Mev is there a difference as large as two standard deviations.

2. Data at 7 Mev and 8 Mev

The data taken near 7 Mev and 8 Mev are not included in Fig. 17 (and will not be included in those to follow) because the uncertainties are too large for the few counts obtained. These data were taken in order to find if there was a large elastic scattering cross section near the photoneutron threshold. It would be expected that the scattering cross section would be small above the threshold (about 7.6 Mev) because neutron emission would dominate. However, large elastic scattering cross sections[42] have been reported for some elements just below neutron threshold. The total photon absorption cross section at 7 Mev might be expected to be about 20 mb;[43] if this estimate is correct, the data show that the elastic scattering cross section is only a small fraction of the inelastic cross section at 7 Mev. This conclusion is consistent[43] with the small level spacing expected at 7 Mev in holmium.

3. Comparison with Other Scattering Data

The data from the three electron counters were combined to obtain better statistics (but poorer resolution). These average data are given in column 7 of Table II, and are plotted as dots in Fig. 18. The open circles are the data obtained by Fuller and Hayward at $\theta = 90^\circ$ (instead of 135° as in this experiment). The dots in Fig. 18 (and Fig. 17) show the gross structure of splitting of the resonance similar to that seen in the absorption cross section by Fuller and Hayward.[3] If both these measurements were correct absolutely, the scattering at 90° would be larger than that at 135°. It seems much more likely that an absolute error exists because other experiments and theory call for a cross section which is proportional to $A + B \cos^2\theta$. The values expected for the scalar part of the scattering are $A = B$, while for the tensor part, $A = 13\ B$.
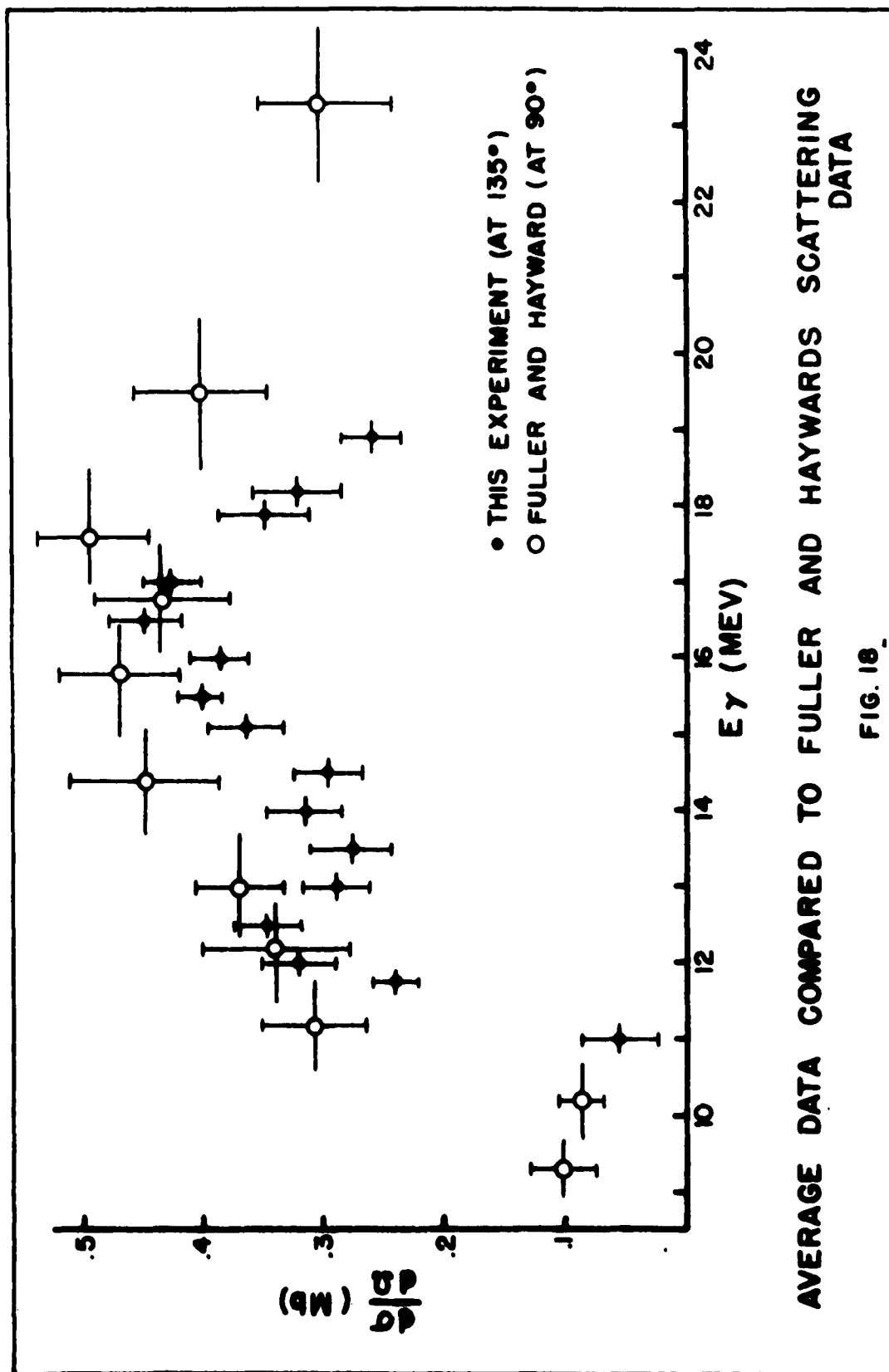
FIG. 18.

AVERAGE DATA COMPARED TO FULLER AND HAYWARDS SCATTERING DATA

- THIS EXPERIMENT (AT 135°)
- ○ FULLER AND HAYWARD (AT 90°)

$E\gamma$ (MEV)

$\frac{d\sigma}{d\Omega}$ (Mb)

If an absolute normalization is made, the data agree over most of the energy range. (The agreement is improved by remembering that the Fuller and Hayward points should be plotted at higher energies than shown for a rising portion of the cross section;[44] furthermore, there may be a slight energy scale discrepancy.) There is some evidence for the 135° data falling more rapidly with energy above 17 Mev. This could be explained if the scattering cross section were not pure electric dipole at these energies. (Pure quadrupole would give considerably less intensity at 135° than at 90°. Interference between quadrupole and dipole scattering might have the same effect in some energy regions.)

4. Comparison with Absorption Data

The forward scattering predicted by the absorption data depends on the mechanism of the absorption, and on whether or not some high energy inelastic scattering is included in the measured cross section. If an axially symmetric nucleus is assumed, and the absorption cross section is given by the sum of two Lorentz lines,

$$\sigma_{abs} = \sigma_a + \sigma_b \tag{39}$$

where

$$\sigma_a = \frac{\sigma_a^0}{1+L_a^2} \ , \qquad L_a = \frac{E_a^2 - E^2}{E \, \Gamma_a}$$

and

$$\sigma_b = \frac{\sigma_b^0}{1+L_b^2} \ , \qquad L_b = \frac{E_b^2 - E^2}{E \, \Gamma_b}$$

the elastic scattering cross section, given by Eq. (18), is

$$\frac{d\sigma}{d\Omega} = \left(\frac{d\sigma}{d\Omega}\right)^S + \left(\frac{d\sigma}{d\Omega}\right)^T \qquad (40)$$

$$\left(\frac{d\sigma}{d\Omega}\right)^S = \left|\frac{A+2B}{3} + D\right|^2 \frac{1+\cos^2\theta}{2} \qquad (41)$$

$$\left(\frac{d\sigma}{d\Omega}\right)^T = \frac{j(2j-1)}{(j+1)(2j+3)} \left|\frac{2}{3}(A-B)\right|^2 \frac{13+\cos^2\theta}{40} \qquad (42)$$

where A and B are (from Eqs. (17) and (19)):

$$\frac{A}{3} = \frac{4\pi E}{\hbar c} \sigma_a (L_a + i)$$

$$\frac{2B}{3} = \frac{4\pi E}{\hbar c} \sigma_a (L_b + i) \cdot \qquad (43)$$

No attempt was made to determine any of the resonance paramenters, E_a, Γ_a, σ_a^0, E_b, Γ_b, or σ_b^0 from the scattering data. Instead, these parameters were taken from the two line fit made by Fuller and Hayward to their absorption data for holmium.[4] Figure 19 shows the prediction for elastic scattering only for a nucleus with $j = 7/2$. The solid line is the predicted value normalized at 16.5 Mev, and the points are the data. The dashed curve is the scalar part which was calculated numerically by Fuller and Hayward from the dispersion relation (Eq. (7) of Chapter II). The tensor part was calculated from Eq. (42). The shaded regions indicate the uncertainties in the scalar cross section due to the uncertainties in the absorption data arising from the neutron multiplicity correction above the (γ, 2n) threshold. The calculated curves were reduced

PREDICTIONS OF ELASTIC
SCATTERING:
——— TOTAL
– – – SCALAR

E_γ (MEV)

$\frac{d\sigma}{d\Omega}$ (Mb)
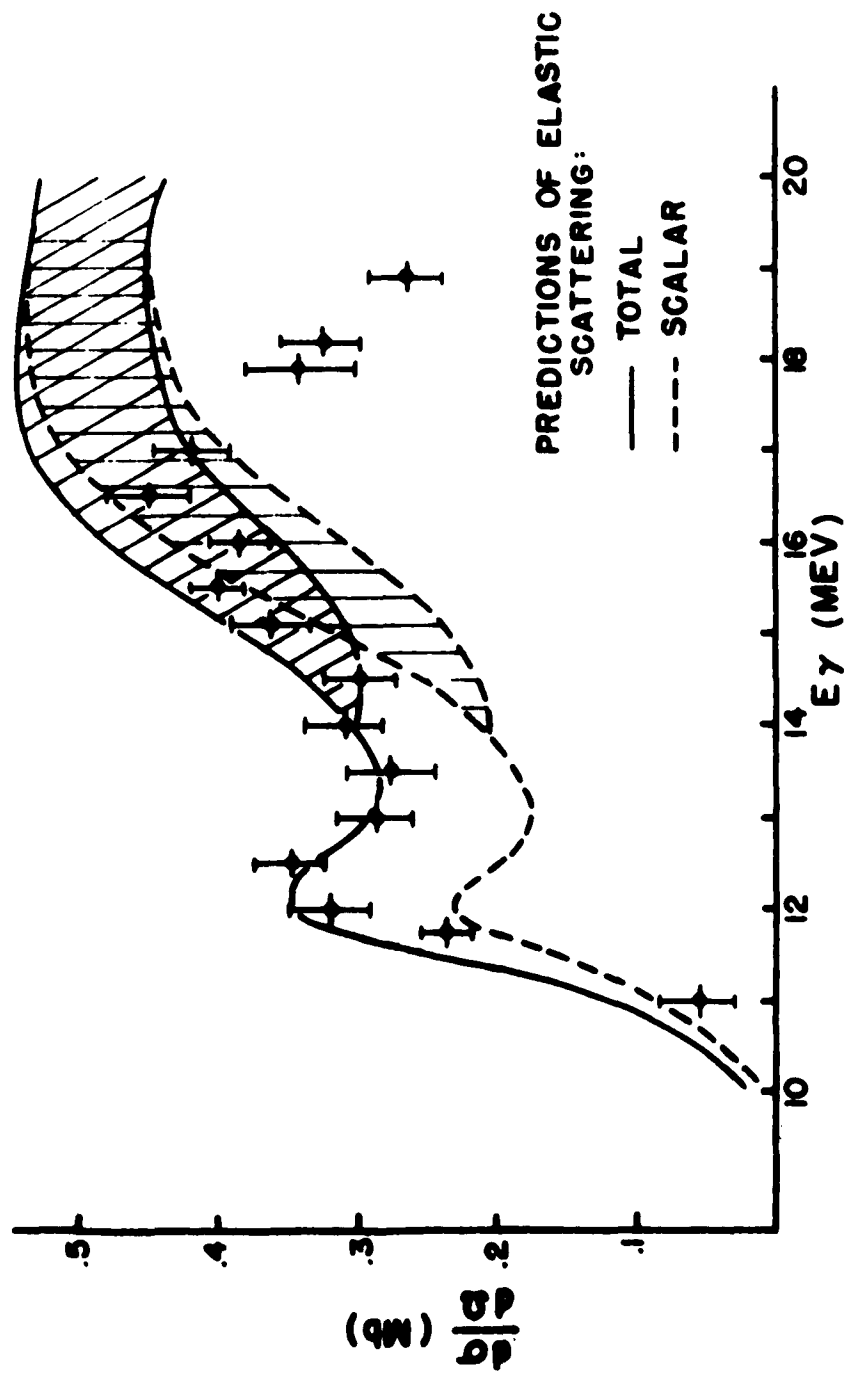
FIG. 19

SCATTERING DATA AND ELASTIC SCATTERING PREDICTION

by 10%. Since, at any energy, the scattering cross section is proportional to the square of the absorption cross section, this is only a 5% reduction in the absorption data. Figure 19 shows that the scalar part alone does not predict the correct energy dependence of the cross section. This is in agreement with the scattering experiments of Fuller and Hayward[45,4] with tantalum, erbium, and holmium. When the tensor elastic scattering is added, the predicted elastic scattering agrees rather well in magnitude and energy dependence with the data for E_γ below 17 Mev. A slight shift in the energy scales would make the agreement even better.

However, Fuller and Hayward found the scattering by erbium (77% of which has spin, $j = 0$) to be identical with that of holmium, indicating that there was no marked dependence of the scattering on nuclear spin. This would be the case if inelastic scattering were included in the measured cross section, for then the spin dependence of the tensor part of the cross section disappears. The tensor cross section for elastic plus inelastic scattering is:

$$\left(\frac{d\sigma}{d\Omega}\right)^T = \left|\frac{2}{3}(A-B)\right|^2 \frac{13+\cos^2\theta}{2} \tag{44}$$

This is the classical expression, and differs from the tensor cross section for purely elastic scattering (Eq. (42)) by the factor,

$\frac{j(2j-1)}{(j+1)(2j+3)}$, which is 0.467 for holmium. Thus the inclusion of inelastic scattering more than doubles the tensor cross section, making the magnitude of the scattering predicted from the absorption cross section considerably larger than the experimental data. Most of the likely complications which arise when scattering data are compared to predictions from absorption data tend to make the predictions too small rather than too large.

If there were other high energy inelastic scattering not associated with the ground state rotational band, but experimentally unresolvable from the elastic scattering, the scattering data would appear higher than the predicted cross section. Also, if there were fine structure in the absorption cross section, the prediction based on the measured average absorption cross section would be too low. [2,46] Thus, if the absolute magnitudes of both the absorption data and the scattering data are correct, there can be no fine structure in the absorption cross section, and no inelastic scattering. (Even if inelastic scattering to the ground state rotational band is not included, the scattering data fall slightly below the prediction from the absorption data, although the 5% reduction in the absorption data needed for normalization is well within the errors of either experiment.) It should be remembered that the optical theorem and dispersion relations predict only the forward scattering cross section while this measurement was done at 135°. The possibility exists that the electric dipole angular distribution assumed is not correct. [2] Since there was a similar discrepancy in the comparison of the magnitudes of these scattering data with those of Fuller and Hayward, it seems likely that an absolute error exists; therefore, the scattering data and the predictions from the absorption data will be normalized at some energy in order to compare their energy dependence.

It can be seen from Fig. 19 that the inclusion of inelastic scattering, which more than doubles the tensor contribution, affects the shape of the predicted cross section as well as the magnitude, since the tensor scattering (calculated from the resonance parameters of Fuller and Hayward's two line fit to their absorption data) is large at energies around 12 and 13 Mev, and decreases rapidly at higher energies. Fuller and Hayward found that they could fit their absorption data equally well with two, or three, Lorentz lines. [4] If the nucleus is assumed to be axially asymmetric, and the

absorption cross section is given by the sum of three Lorentz lines,

$$\sigma_{abs} = \sigma_a + \sigma_b + \sigma_c \qquad (45)$$
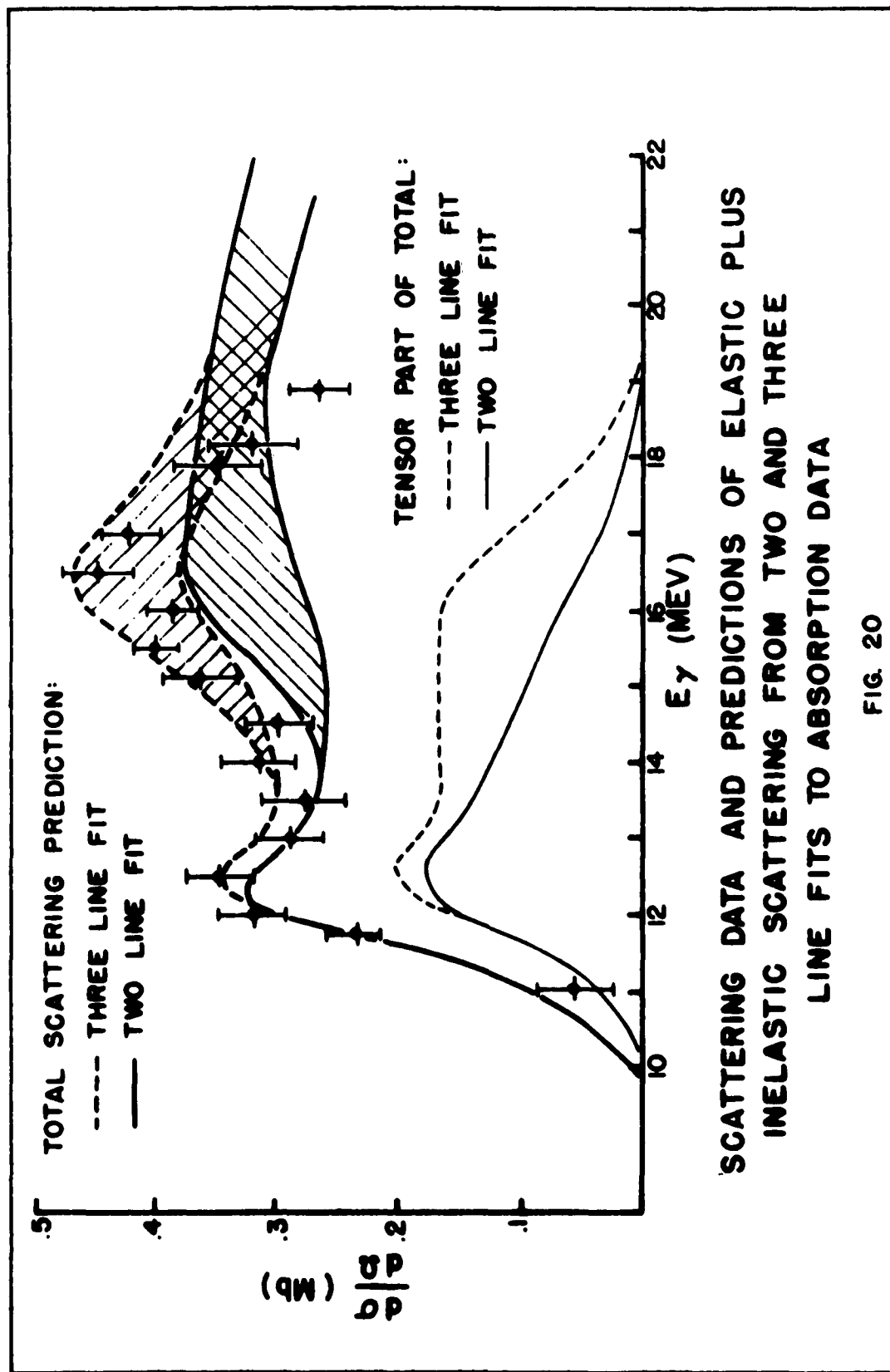
the tensor scattering, from Eq. (24), is:

$$\left(\frac{d\sigma}{d\Omega}\right)^T = \left\{ \left|A-B\right|^2 + \left|B-C\right|^2 + \left|C-A\right|^2 \right\} \frac{13+\cos^2\theta}{180}$$

$$(46)$$

where

$$\frac{A}{3} = \frac{4\pi E}{\hbar c} \sigma_a (L_a + i) \qquad (47)$$

with similar equations for B and C.

Figure 20 shows the elastic plus inelastic scattering predictions for an axially symmetric nucleus (heavy solid line), and a non-axially symmetric nucleus (heavy dashed line), normalized to the data at 11.73 Mev. These curves were obtained by adding the scalar part of the scattering cross section (dashed curve in Fig. 19) to the tensor parts calculated from Eqs. (44) and (46) using the parameters of the 2 and 3 line fits made by Fuller and Hayward to their absorption data. The predicted curves were reduced by 38% (corresponding to a reduction of 19% in the absorption data) and shifted 0.1 Mev toward higher energy. The tensor contributions are shown separately; the light solid line is for the axially symmetric nucleus, and the light dashed line is for the non-axially symmetric nucleus. The scattering data show a slight preference for the prediction from the 3 line fit because of the larger cross section around 16 Mev than at 12 Mev, and the decreasing cross section above

FIG. 20

SCATTERING DATA AND PREDICTIONS OF ELASTIC PLUS
INELASTIC SCATTERING FROM TWO AND THREE
LINE FITS TO ABSORPTION DATA

17 Mev. A definite choice between these two sets of parameters cannot be made at this time because of the large uncertainties in the absorption cross section above 14 Mev, and because of the rather large normalization needed to obtain agreement in the magnitudes of the two measurements. It is important to know more precisely the absorption cross section, particularly above 14 Mev, and to resolve the discrepancy in the magnitudes; then the requirement that the same resonance parameters predict both the absorption cross section and the scattering cross section would severely limit the choice of parameters.

It was pointed out in Chapter II, and in reference 4, that the asymmetry parameter,γ , of 20°, implied by this particular three resonance line fit, is larger than expected even if holmium had a permanent non-axially symmetric deformation. However, a two line fit to the absorption and scattering data is unrealistic even for an axially symmetric nucleus, because the agreed upon zero-point vibrations are ignored. From a consideration of the zero-point γ vibrations, a three line fit would be expected even for a nucleus with no permanent axial asymmetry. The zero-point β vibrations should also be considered. In order to estimate, crudely, the possible effect of these γ vibrations on the scattering cross section, the tensor scattering cross section has been calculated at 16 Mev as a function of using the resonance parameters: E_a = 12 Mev, Γ_a = 2 Mev, σ_a^0 = 319 mb;

E_b = (15.5 -x) Mev, Γ_b = 3 Mev, σ_b^0 = 213 mb; and E_c = (15.5 + x) Mev,

Γ_c = 3 Mev, σ_c^0 = 213 mb, for values of x from 0 to 1 Mev, giving values of γ from 0° to about 20°. The values of γ were calculated using Eqs. (2) and (3). (At x = 1 Mev, these parameters are identical to Fuller and Hayward's three line fit. At x = 0, they differ slightly from Fuller and Hayward's two line fit, because their second resonance line has a

width of 4 Mev rather than 3 Mev, and a peak of 319 mb rather than 426 mb.)
Figure 21 shows the percentage increase in the tensor scattering at 16 Mev
as a function of γ . The increase is roughly linear with γ . If 13° is taken
for the root mean square γ , due to zero-point oscillations, and the wave
function is assumed proportional to $e^{-a\gamma^2}$, the average of $|\gamma|$ is about
10.5°. From Fig. 21, this gives an increase in the tensor scattering of
about 30%. This estimate gives a tensor scattering prediction of 0.13 mb
at 16 Mev (compared to the value of 0.17 mb from the three line fit with
$\gamma = 20°$). Since the scalar part is about 0.28 mb at 16 Mev (with the normaliza-
tion in Fig. 20), this estimate gives a prediction of 0.41 mb which agrees
well with the data. This rough estimate illustrates the effects on the tensor
scattering cross section to be expected if the zero-point γ vibrations are
included in the hydrodynamic model. If the hydrodynamic model is applicable,
the zero-point β and γ vibrations should be included.

Although Fig. 19 shows that the scattering data are in good agreement
with the elastic scattering cross section prediction from the absorption data
assuming an axially symmetric nucleus (and ignoring zero-point vibrations),
the experiments of Fuller and Hayward with erbium and holmium imply that
some inelastic scattering is included in the measured cross section. When
this inelastic scattering is included, the scattering data fall below this pre-
diction, and the agreement in the energy dependence is not as good, although
the large uncertainties in the absorption cross section at high energies make
the comparison difficult. An equivalent interpretation of the absorption
data ("equivalent" as far as agreement with the absorption data is
concerned), assuming a non-axially symmetric nucleus (and ignoring
zero-point vibrations) leads to a prediction of the energy dependence of
the scattering cross section which agrees better with the data, however,

EFFECT OF AXIAL ASYMMETRY ON
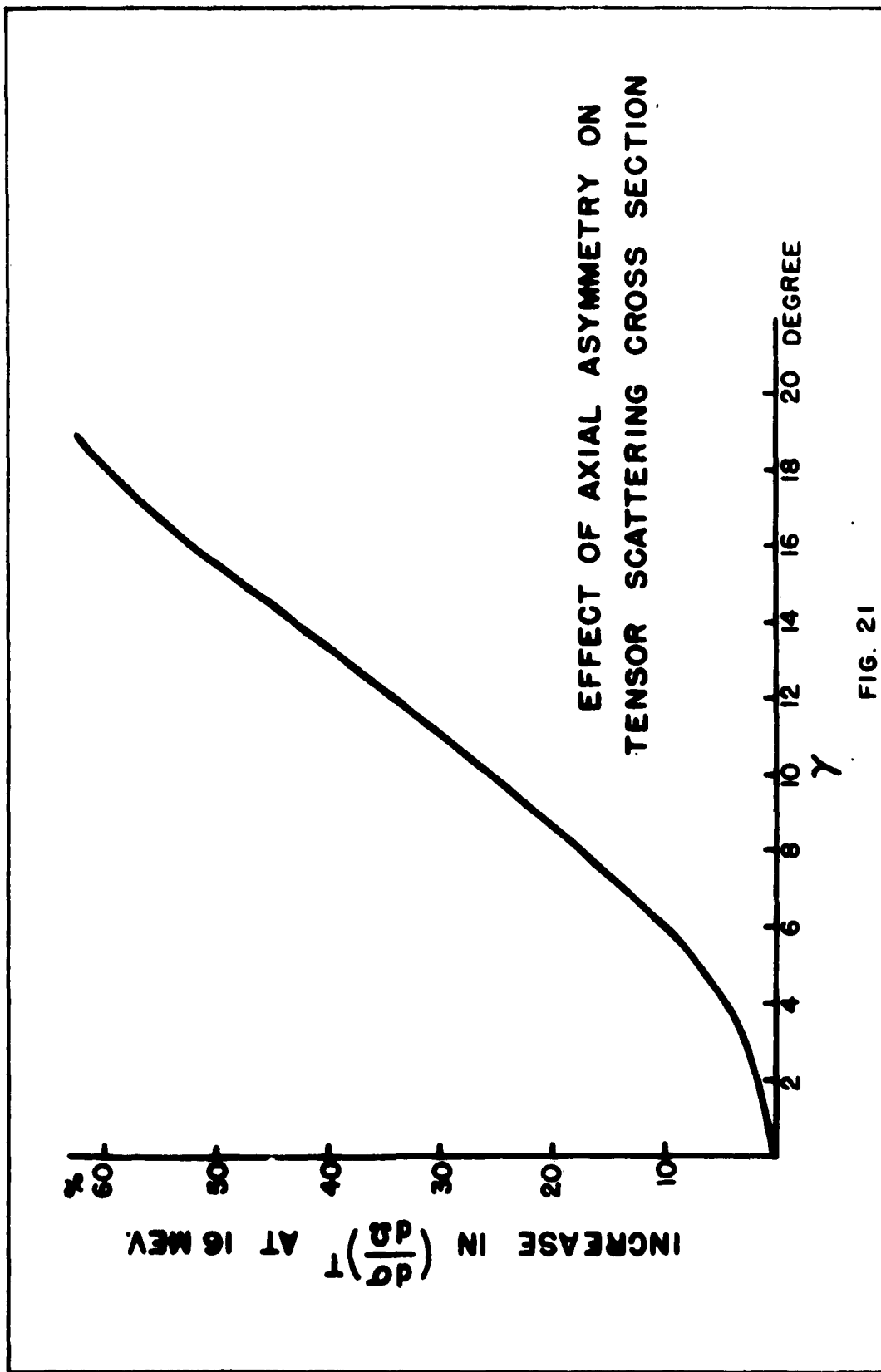TENSOR SCATTERING CROSS SECTION

FIG. 21

the axial asymmetry implied by this interpretation is unrealistically large. The simplest interpretation of this scattering data is that: (1) Some inelastic scattering is present, and the discrepancy between the magnitudes of the scattering data and the cross section predicted from the absorption data is due to an absolute error in one of the measurements. (If the scattering data are correct, the absorption data are about 20% too high, while if the absorption data are correct, the scattering data are about 40% too low.) (2) Reasonable agreement between the energy dependence of the scattering data and the predicted cross section can be obtained by including the effects of zero-point vibrations of either an axially symmetric nucleus, or a nucleus with a more reasonable axially asymmetry than given by $\gamma = 20^{\circ}$.

BIBLIOGRAPHY

1. J. S. O'Connell, P. Tipler, and P. Axel, "The Bremsstrahlung Monochromator," Technical Report No. 21, Office of Naval Research Contract Nonr 1834(05).

2. J. S. O'Connell, P. Tipler, and P. Axel, "The Elastic Scattering of 11.5 - 17.7 Mev Photons by Au Measured with a Bremsstrahlung Monochromator (to be published).

3. E. G. Fuller and E. Hayward, Proceedings of the International Conference on Nuclear Structure. Edited by D. Bromley and E. Vogt. University of Toronto Press, Toronto (1960), p. 760 and p. 763.

4. E. G. Fuller and E. Hayward, "The Nuclear Photoeffect in Holmium and Erbium." National Bureau of Standards, Washington, D. C.

5. J. S. Levinger, Nuclear Photo-Disintegration. Oxford University Press (1960), p. 35 and p. 26.

6. D. H. Wilkinson, Annual Review of Nuclear Science. Edited by E. Segre. Annual Reviews, Inc., California (1959), Vol. 9, p. 1.

7. G. Cotte, W. Turchinetz, and I. Wright, Nuclear Physics 23, 468 (1961).

8. M. Danos, Ann. Phys. 10, 265 (1952).

9. K. Okamoto, Progr. Theoret. Phys. (Japan) 15, 75 (1956).

10. M. Goldhaber and E. Teller, Phys. Rev. 74, 1046 (1948).

11. H. Steinwedel, J. H. D. Jensen, and P. Jensen, Z. Naturforsch. 5a, 423 (1950).

12. K. Okamoto, Phys. Rev. 110, 143 (1958).

13. D. H. Wilkinson, Phil. Mag. 3, 567 (1958).

14. M. Soga and J. Fujita, Nuovo cimento 6, 1494 (1957).

15. B. Mottelson and S. Nilsson, Nuclear Phys. 13, 281 (1959).

16. G. E. Brown and M. Bolsterli, Phys. Rev. Letters 3, 472 (1959).

17. G. E. Brown, L. Castillejo, and J. Evans, Nuclear Phys. 22, 1 (1961).

18. E. G. Fuller and M. S. Wiess, Phys. Rev. 112, 560 (1958).

19. M. Danos, Nuclear Phys. 5, 23 (1958).

20. B. Spicer et al., Australian J. Phys. 11, 298 (1958).

21. P. Flournoy, R. Tickle, and W. Whitehead, Phys. Rev. 120, 1424 (1961).

22. E. Inopin, Soviet Phys. --JETP (trans.) 38, 992 (1960).

23. A. Davydov and G. Filippov, Soviet Phys. --JETP (trans.) 35, 440 (1958).

24. A. Davydov and G. Filippov, Nuclear Phys. 8, 237 (1958).

25. A. Bohr and B. Mottelson, Mat. Fys. Medd. Dan. Vid. Selsk. 27, No. 16 (1953).

26. Proceedings of the International Conference on Nuclear Structure. Edited by D. Bromley and E. Vogt. University of Toronto Press, Toronto (1960), p. 801 ff, p. 807 ff, and p. 898 ff.

27. D. R. Bes, Mat. Fys. Medd. Dan. Vid. Selsk. 33, No. 2 (1961).

28. Gell-Mann, Golberger, and Thirring, Phys. Rev. 95, 1612 (1954).

29. A. Baldin, Nuclear Phys. 9, 237 (1959).

30. A. Baldin, Soviet Phys. --JETP (trans.) 37, 202 (1960).

31. G. Placzek, Marx Handbuch der Radiologie 6, Part 2, 205 (1934).

32. Z. Maric and P. Mobius, Nuclear Phys. 10, 135 (1959).

33. S. Bhagavantam, Scattering of Light and the Raman Effect. Chemical Publishing Co., Brooklyn (1942), 1st American Edition.

34. F. Ajzenberg-Selove and T. Lauritsen, Nuclear Phys. 11, 1 (1959).

35. P. M. Endt, private communication.

36. P. Axel, University of Illinois Report 22, 1961 (unpublished).

37. J. Miller, Centre d'etudes Nucleaires de Saclay, Report CEA No. 655.

38. R. Gluckstern and M. Hull, Phys. Rev. 90, 1030 (1953).

39. G. White Grodstein, National Bureau of Standards Circular No. 583. U. S. Government Printing Office, Washington, D. C. (1957).

40. W. Miller and W. Snow, Rev. Sci. Instr. 31, 39 (1960).

41. W. Miller and W. Snow, "Monte Carlo Calculation of the Energy Loss Spectra for Gamma Rays in Sodium Iodide and Cesium Iodide," ANL-6310, Argonne National Laboratory (unpublished); and private communication.

42. E. G. Fuller and E. Hayward, Phys. Rev. 101, 692 (1956).

43. P. Axel, to be published.

44. E. G. Fuller and E. Hayward, to be published.

45. E. G. Fuller and E. Hayward, Phys. Rev. Letters 1, 1507 (1958).

46. A. Penfold and E. Garwin, Phys. Rev. 116, 120 (1959).